

# KIC 4150611: A quadruply eclipsing heptuple star system with a g-mode period-spacing pattern

## Asteroseismic modelling of the g-mode period-spacing pattern

Alex Kemp<sup>1\*</sup>, Dario J. Fritzewski<sup>1</sup>, Timothy Van Reeth<sup>1</sup>, Luc IJspeert<sup>1</sup>, Mathias Michielsen<sup>1</sup>, Joey S. G. Mombarg<sup>2</sup>, Vincent Vanlaer<sup>1</sup>, Gang Li<sup>1</sup>, Andrew Tkachenko<sup>1</sup>, and Conny Aerts<sup>1,3,4</sup>

<sup>1</sup> Institute of Astronomy (IvS), KU Leuven, Celestijnenlaan 200D, 3001, Leuven, Belgium

<sup>2</sup> IRAP, Université de Toulouse, CNRS, UPS, CNES, 14 Avenue Édouard Belin, 31400 Toulouse, France

<sup>3</sup> Department of Astrophysics, IMAPP, Radboud University Nijmegen, PO Box 9010, 6500 GL Nijmegen, The Netherlands

<sup>4</sup> Max Planck Institute for Astronomy, Königstuhl 17, 69117 Heidelberg, Germany

### ABSTRACT

**Context.** KIC 4150611 is a high-order (seven) multiple composed of a triple system with: a F1V primary (Aa), which is eclipsed on a 94.2d period by a tight binary composed of two K/M dwarfs (Ab1, Ab2), which also eclipse each other; an eccentric, eclipsing binary composed of two G stars (Ba, Bb); and another faint eclipsing binary composed of two stars of unknown spectral type (Ca and Cb). In addition to its many eclipses, the system is an SB3 spectroscopic multiple (Aa, Ba, and Bb) and the primary (Aa) is a hybrid pulsator, exhibiting high amplitude pressure and gravity modes (g-modes). Further, its g-modes are arrayed in a period-spacing pattern, which greatly assists with mode identification and asteroseismic modelling. In aggregate, this richness in physics offers an excellent opportunity to obtain a precise physical characterisation for some of the stars in this system.

**Aims.** In this work, we aim to estimate the stellar parameters of the primary (Aa) by performing asteroseismic analysis on its period-spacing pattern.

**Methods.** We use the C-3P0 neural network to perform asteroseismic modelling of the g-mode period-spacing pattern of Aa, discussing the interplay of this information with external constraints from spectroscopy ( $T_{\text{eff}}$  and  $\log(g)$ ) and eclipse modelling ( $R$ ). To estimate the level of uncertainty due to different frequency extraction and pattern identification processes, we consider four different variations on the period-spacing patterns. To better understand the correlations between and the uncertainty structure of our parameter estimates, we also employed a classical, parameter-based MCMC grid search on four different stellar grids.

**Results.** The best-fitting, externally constrained model to the period-spacing pattern arrives at estimates of the stellar properties for Aa of:  $M=1.51 \pm 0.05 M_{\odot}$ ,  $X_c=0.43 \pm 0.04$ ,  $R=1.66 \pm 0.1 R_{\odot}$ ,  $f_{\text{ov}}=0.010$ ,  $\Omega_c=1.58 \pm 0.01 \text{ d}^{-1}$  with rigid rotation to within the measurement errors,  $\log(T_{\text{eff}})=3.856 \pm 0.008 \text{ dex}$ ,  $\log(g)=4.18 \pm 0.04 \text{ dex}$ , and  $\log(L)=0.809 \pm 0.005 \text{ dex}$ , which agree well with previous measurements from eclipse modelling, spectroscopy, and the *Gaia* DR3 luminosity.

**Conclusions.** We find that the near-core properties of the best-fitting asteroseismic models are consistent with external constraints from eclipse modelling and spectroscopy. For stellar properties not relating to the near-core region, external constraints on the asteroseismic best-fitting models are informative. Aa appears to be a typical example of a  $\gamma$  Dor star, fitting well within existing populations. We find that Aa is quasi-rigidly rotating to within the uncertainties, and note that the asteroseismic age estimate for Aa ( $1100 \pm 100 \text{ Myr}$ ) is considerably older than the young (35 Myr) age implied by previous isochrone fits to the B binary in the literature. Our MCMC parameter-based grid-search agrees well with our pattern-modelling approach. Improved future modelling may come from detailed coverage of metallicity effects and careful treatment of envelope physics.

**Key words.** Stars, binaries: eclipsing, binaries: spectroscopic, asteroseismology, stars: oscillations

## 1. Introduction

Asteroseismology, the study of stellar oscillations, stands as a cornerstone in modern astrophysics, offering unique insights into fundamental stellar properties. The sensitivity of stellar oscillation frequencies to the interior structure has opened the door to the measurement of stellar properties that are beyond the reach of surface observations. We can exploit this direct link between theoretical models and observations to refine our understanding of stellar evolution (Aerts 2021).

Asteroseismology's role in modern astrophysics has grown rapidly since the advent of space-based planet-hunting surveys such as CoRoT (Baglin 2003), *Kepler* (Borucki et al. 2010), and

TESS (Ricker et al. 2015), which provided near-uninterrupted, high-precision photometry with regular cadence on long time-bases. One outcome of this new era of space-based photometry has been the detection of low-frequency gravity-modes (g-modes) in large numbers of stars (Van Reeth et al. 2015a,b; Li et al. 2019b,a). Previously, this had been impossible due to the logistical challenges of obtaining long time base data for even a small number of stars (e.g., De Cat & Aerts 2002; Aerts et al. 2004; De Cat et al. 2006). Gravity-mode (g-mode) oscillations are waves that propagate with buoyancy as the dominant restoring force, and are particularly sensitive to the near-core stellar properties (Miglio et al. 2008). Pressure modes (p-modes) have pressure as their dominant restoring force and have higher frequency. These modes are more sensitive to bulk stellar properties

\* e-mail: alex.kemp@kuleuven.be

such as the average stellar density and envelope properties such as rotation (Aerts et al. 2010).

In order for stellar oscillations to be observed, they must propagate to the surface where they produce variations in the stellar flux. Main sequence stars more massive than approximately  $1.2 M_{\odot}$  have a convective core and a radiative envelope. As g-modes are restored by buoyancy, they can propagate through the radiative envelope from the near-core region to the surface, where they are observed, but not within the convective stellar core.

Stars with masses between approximately  $1.4 M_{\odot}$  and  $1.9 M_{\odot}$  with observed g-mode pulsations are known as  $\gamma$  Doradus ( $\gamma$  Dor) pulsators, and feature g-mode pulsations excited via convective flux blocking (Dupret et al. 2005). Some  $\gamma$  Dor stars have overlap with the  $\delta$  Scuti ( $\delta$  Sct) stars, which typically have masses between  $1.5$  and  $2.5 M_{\odot}$ , and exhibit p-mode oscillations driven by the opacity-driven heat engine mechanism.

The primary component of KIC 4150611<sup>1</sup> is an example of a  $\gamma$  Dor/ $\delta$  Sct hybrid pulsator: a star which exhibits both  $\delta$  Sct and  $\gamma$  Dor pulsations (Uytterhoeven et al. 2011). In this work, we focus our analysis attention on modelling the g-mode period-spacing pattern. The prominent p-mode pulsations do not form a part of this analysis, as without mode identification they provide negligible constraining power – but add significant modelling complexity – to the analysis. Analysis of the p-mode  $\delta$  Sct pulsations can be found in Shibahashi & Kurtz (2012) and Balona (2014).

KIC 4150611 is a high-order (seven) multiple star system with four different sets of eclipses. The primary, Aa, is a bright ( $V \approx 8$  mag) F1V-type star that is in an eclipsing 94.2d circular orbit with a 1.52d self-eclipsing binary (Ab) composed of two dim (negligible light contribution) K/M dwarf stars (Ab1 and Ab2). The resulting primary eclipses of the triple geometry are complicated, varying significantly between eclipses depending on the phase of the Ab binary. Associated on roughly a 1000 yr orbit with the A triple is the eccentric 8.65d eclipsing B binary, composed of two near-identical G-type stars, Ba and Bb. The final component of the candidate heptuple is the C binary, a 1.43d eclipsing binary composed of two stars of unknown spectral type, Ca and Cb. If the C binary is indeed dynamically associated with the A-B quintuple – and therefore at approximately the same distance from the observer – their negligible contribution to the total flux implies that they are likely also cool dwarfs. The system structure is summarised in Fig. 1.

The system structure described above was established in Helminiak et al. (2017), who conducted velocity modelling of Aa, Ba, and Bb as well as eclipse modelling of the Ab, B, and C binaries. The authors further performed imaging of the system using adaptive optics which established it as a visual triple, astrometric measurements searching for long-period dynamical associations, and isochrone fitting based on the properties of Ba and Bb. Detailed eclipse modelling of the A triple can be found in Kemp et al. (2024), along with spectroscopic analysis and atmospheric modelling of the disentangled spectra of Aa, Ba, and Bb.

In this work, we build on the previous eclipse and atmospheric analysis of Aa to perform asteroseismic modelling of its g-mode period-spacing pattern, first identified in Li et al. (2020a). G-mode period-spacing patterns are sensitive to interior stellar properties such as near-core rotation rates and buoyancy travel times (Van Reeth et al. 2016; Mombarg et al. 2019),

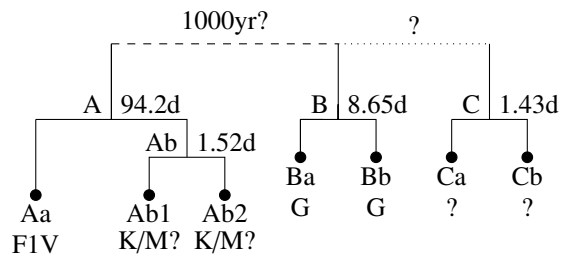


Fig. 1: Summarising the system hierarchy and nomenclature of KIC 4150611, with approximate orbital periods shown in days. Helminiak et al. (2017) present astrometric evidence for an association between the A and B components, but otherwise the A, B, and C components can be considered dynamically independent. Figure is based on Figure 15 from Helminiak et al. (2017).

and when combined with grids of stellar models with computed pulsations, can be used to estimate stellar properties such as masses, ages, and mixing profiles (see, for example, Aerts et al. 2018; Johnston et al. 2019; Pedersen et al. 2021; Mombarg et al. 2021; Michielsen et al. 2023). By considering several different period-spacing patterns and by employing both a pattern-matching approach and parameter-based grid-search approach that leverages different grids of stellar models, we aim to provide insight into the systematic uncertainty associated with different methods and choices. Attention is also paid to how the different non-asteroseismic measurements that have been made for this system interplay with both each-other and the asteroseismology.

We provide a summary of physical constraints relevant to the asteroseismic modelling of KIC 4150611’s g-mode period-spacing pattern in Section 2. We describe our methodology in Section 3, and present our results in Section 4. We conclude in Section 5.

## 2. Physical constraints from previous literature

In this section, we provide a brief summary of selected constraints on orbital and stellar properties from the literature relevant to the asteroseismic modelling of Aa. Much of the previous literature relating to KIC 4150611 is dedicated to constraining the orbital properties of the system. These constraints are essential to the identification and extraction of stellar oscillation frequencies as they allow confident identification of orbital harmonics (see Section 3.1).

Using a variety of techniques, several works have provided estimates of the orbital periods of KIC 4150611’s different components (Prša et al. 2011; Shibahashi & Kurtz 2012; Balona 2014; Rowe et al. 2015; Helminiak et al. 2017; Kemp et al. 2024). For the Ab, B, and C binaries, we make use of the orbital periods from Helminiak et al. (2017) to aid the identification of orbital harmonics. The complex, time-variant geometry of the 94.2d eclipses precludes harmonic analysis; these eclipses are removed from the light curve in the time domain before the Fourier-space frequency analysis commences.

From *Gaia* DR3 (Gaia Collaboration et al. 2023), we have an estimate for the distance to the system of  $123.6^{+1.6}_{-2.3}$  pc<sup>2</sup>, which (using a bolometric<sup>3</sup> magnitude of 8.03 for the system) in turn

<sup>2</sup> from *Gaia*’s distance\_gspphot label.

<sup>3</sup> The bolometric correction is taken to be +0.01, see [https://www.pas.rochester.edu/%7Eemamajek/EEM\\_dwarf\\_UBVIJHK\\_colors\\_Teff.txt](https://www.pas.rochester.edu/%7Eemamajek/EEM_dwarf_UBVIJHK_colors_Teff.txt) (Pecaut & Mamajek 2013)

<sup>1</sup> HD 141469; RA=19° 18′ 58.21759", DEC=+39° 16′ 01.7913" (J2000)

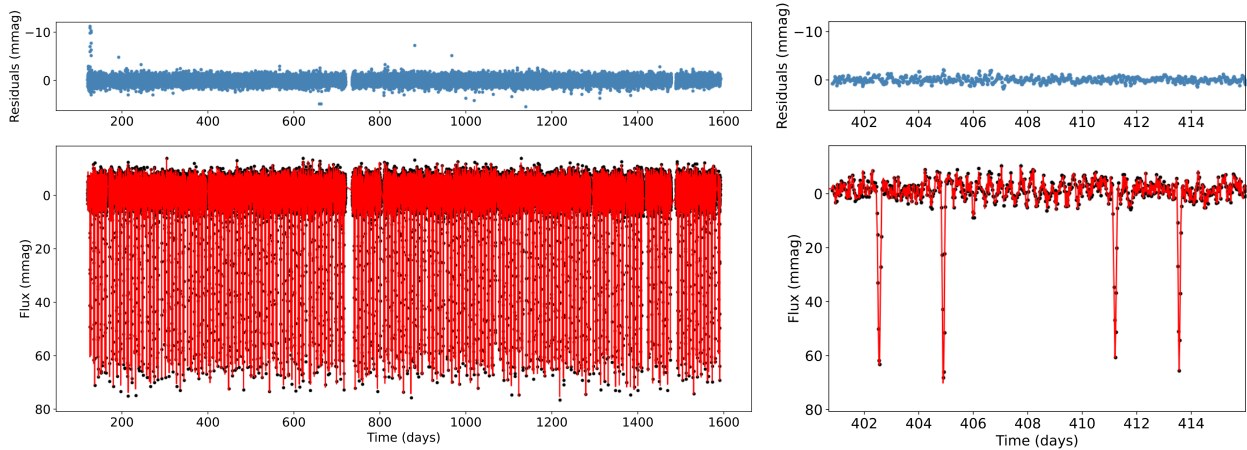


Fig. 2: The bottom panel shows the normalised, detrended light curve (black) (excepting 94.2d eclipses) and the sinusoid model (red) formed from all frequencies extracted using STAR SHADOW. The upper panel shows the residuals (blue). Figure 1 of Kemp et al. (2024) shows the equivalent figure for the period04 extraction.

provides an estimate for the system’s luminosity of  $7.5 \pm 0.3 L_{\odot}$  ( $\log(L) = 0.875 \pm 0.0175$  dex). To make the step from a system luminosity to a stellar luminosity for Aa, we must consider the light fraction of Aa in the system.

The primary makes up most of the light in the system, although estimates of the exact light fraction vary. Kemp et al. (2024) estimate a light fraction of between 0.92 and 0.94 based on spectroscopic analysis of TRES (Szentgyorgyi & Furész 2007) spectra, but arrive at a lower value of roughly  $0.84 \pm 0.03$  when considering only the eclipses, a value similar to the 0.85 light fraction obtained by Helminiak et al. (2017) in their eclipse modelling of the Ab, B, and C binaries. Kemp et al. (2024) consider the effect of this uncertainty on their estimates of system’s properties from their eclipse analysis, noting that the spectroscopic analysis appears far more sensitive to the light fraction than the eclipse modelling and therefore prefer a light fraction of around 0.92. A light fraction of 0.85 implies a  $\log(L)$  for Aa of  $0.804 \pm 0.017$  dex, while a light fraction of 0.92 implies a  $\log(L)$  for Aa of  $0.838 \pm 0.017$  dex. Note that the quoted uncertainties only propagate the uncertainty in parallax, and so are lower limits.

From the eclipse modelling in Kemp et al. (2024), the stellar radius for Aa was conservatively estimated as  $1.64 \pm 0.06 R_{\odot}$  when considering the possibility of either a low or high light fraction being true. Each of Kemp et al. (2024)’s two Markov Chain Monte Carlo (MCMC) simulations with constrained light fractions arrive at  $1-\sigma$  uncertainties of approximately  $0.01 R_{\odot}$ .

Helminiak et al. (2017) provide estimates of several of the properties of Aa properties using isochrone fits to Ba and Bb. These properties include the mass ( $1.64 \pm 0.06 M_{\odot}$ ), radius ( $1.376 \pm 0.013 R_{\odot}$ ),  $\log(g)$  ( $4.38 \pm 0.01$  dex), and effective temperature ( $8440 \pm 280$  K). However, isochrone fits suffer from high levels of modelling uncertainty, being tied to the underlying grid of stellar models. Kemp et al. (2024) found poor agreement between their eclipse modelling and the stellar properties estimated from the isochrone fits of Helminiak et al. (2017), including the radius and mass ratio estimates for the Aa, Ab1, and Ab2 components of the A triple. The effective temperature ( $T_{\text{eff}}$ ) of Aa from the isochrone fits is also too high compared to both the atmospheric modelling conducted in Kemp et al. (2024) and previous spectroscopic analysis from Niemczura et al. (2015). The

properties from the isochrone fits we use only for comparative purposes.

The atmospheric modelling on the disentangled spectra of Aa presented in Kemp et al. (2024) estimate  $T_{\text{eff}} = 7280 \pm 70$  K and  $\log(g) = 4.14 \pm 0.18$  dex. From the eclipse modelling, there is a deviation from edge-on of at most  $0.4^{\circ}$ , so the estimate of  $v \sin i = 127 \pm 4 \text{ km s}^{-1}$  can be considered simply as the surface rotation. Combined with the conservative estimate of the stellar radius of  $1.64 \pm 0.06 R_{\odot}$  from the eclipse modelling (Kemp et al. 2024), this corresponds to an estimate on the rotation frequency of the surface,  $\Omega_{\text{surf}}$ , of  $1.54 \pm 0.1 \text{ d}^{-1}$ , where the quoted error encompasses the highest level of disagreement permissible within the  $1-\sigma$  of the radius and surface rotation constraints.

### 3. Methodology

#### 3.1. Frequency extraction

The process of detrending and obtaining frequencies from KIC 4150611’s complicated photometric time series was discussed in Kemp et al. (2024), but we summarise it again here, as it gives important context to three of the four period-spacing patterns we consider (see Section 3.3).

For the purpose of obtaining a g-mode period-spacing pattern for a  $\gamma$  Dor star, *Kepler*’s long-cadence time-series data can be considered ideal. KIC 4150611 is sparsely observed by TESS and has considerably poorer signal-to-noise, while short-cadence *Kepler* data offers little benefit to the low-frequency g-modes of  $\gamma$  Dor stars but adds to the computational cost considerably.

Starting from the *Kepler* long-cadence target-pixel-files (TPFs), we employ a custom reduction and instrumental detrending following Van Reeth et al. (2022, 2023). The procedure is designed to improve the available signal while minimising contaminants from other stellar sources and avoid introducing signal from the instrumental detrending. This is achieved by applying a simple linear detrending model to each sector after a rough sinusoid model for the dominant physical effects (typically either eclipses or oscillations) has been subtracted. This is followed by outlier removal through a  $5-\sigma$  clipping and manual inspection. Throughout the detrending process, the 94.2d eclipses of the A triple were removed from the light-curve. In principle they could

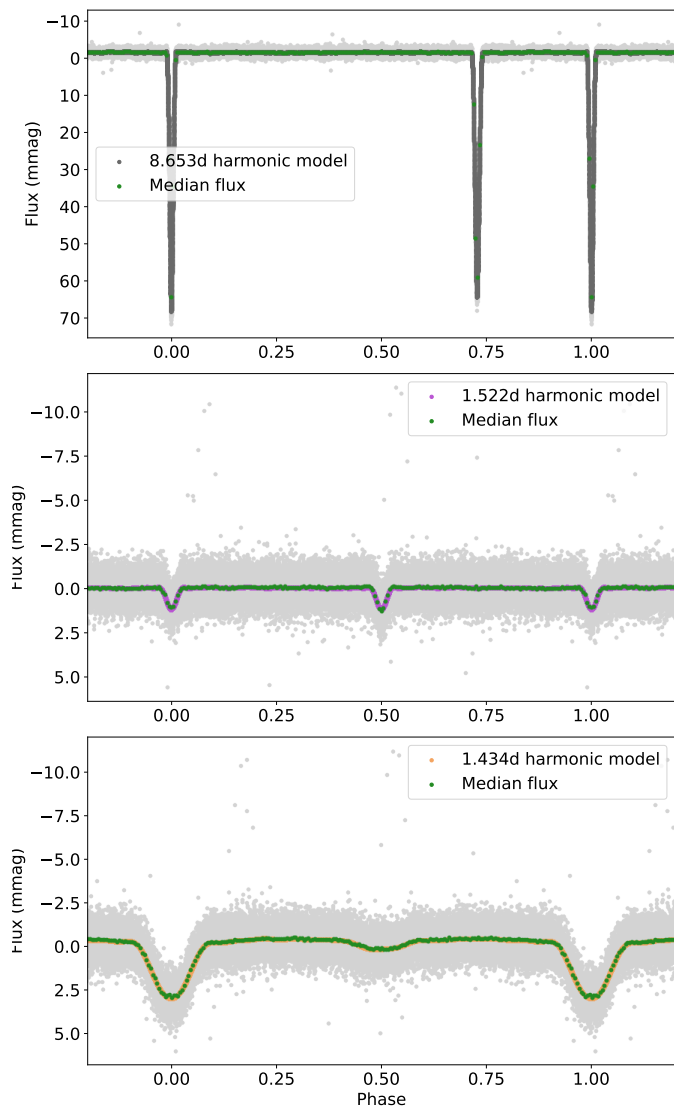


Fig. 3: Phase-folded light curves for each of the eclipsing components and its sinusoid model. The light curve (grey data) for each is the residual between the normalised, detrended light curve and every frequency except those forming the sinusoid model of the relevant eclipse from STAR SHADOW. The median flux is shown in green, while the coloured (colour varies by panel) points are from relevant harmonic model. Fig. 3 of Kemp et al. (2024) shows the equivalent figure for the `period04` extraction, with no significant differences to the eclipse geometry.

be reintroduced and detrended once the detrending curve was obtained, however, prewhitening in the frequency domain with these complicated eclipses included in the light curve is impractical and counterproductive.

To obtain lists of frequencies, amplitudes, and phases we iteratively prewhiten the detrended light curve (with the 94.2d eclipses removed) using two different methods: manually using `period04`<sup>4</sup>, and in an automated way using STAR SHADOW<sup>5</sup> (IJspeert et al. 2024). Further details of this procedure can be found in Section 2.1.1 of Kemp et al. (2024), and the detrended light-curve – and model fit using the STAR SHADOW frequency

model – can be seen in Fig. 2. However, it is relevant to highlight certain key differences between the two processes.

The first is that while both methods identify orbital harmonics of the 8.65d, 1.52d, and 1.43d eclipses, only STAR SHADOW couples the orbital frequencies for all identified harmonics, leading to a more precise extraction of orbital harmonics. This has relevance due to a near-perfect coincidence between an 8.65d orbital harmonic and one of the g-modes of KIC 41501611. Fig. 3 shows the phase-folded orbital periods using the STAR SHADOW frequencies, and can be compared directly to Figure 3 from Kemp et al. (2024) and Figure 2 from Helminiak et al. (2017), highlighting the consistency of the eclipse extraction.

The second difference worth highlighting is that, as an automated method, STAR SHADOW employs a strict amplitude-hinting procedure (see, for example, Van Beeck et al. 2021). This means that it proceeds with iterative frequency extraction in descending amplitude order, stopping as soon as the Bayes information criterion reduces by less than two when extracting the next frequency. In contrast, when prewhitening using `period04` the selection of the prewhitened frequencies is at the discretion of the user, as is the point at which to stop the process. For discussion on different prewhitening procedures and the influences they can have on the resulting frequency lists, the reader may refer to Degroote et al. (2009) and Van Beeck et al. (2021).

The presence of low-frequency noise in the Fourier transform (commonly referred to as ‘red noise’) can cause frequency extraction to halt before reaching low amplitude – but high SNR – frequencies in the high-frequency domain. This results in the extraction of a lower number of frequencies overall, with high-frequency orbital harmonics clearly appearing in the residuals (see Figs. 4 and 5). The lack of these frequencies appear to have little bearing on the quality of the orbital harmonic models, however, nor on the quality of the pre-whitening in the g-mode regime.

Manual extraction using `period04` results in 178 orbital harmonics for the 8.65d orbital period, 18 orbital harmonics for the 1.52d orbital period, 19 orbital harmonics for the 1.43d orbital period, and 1238 other frequencies. STAR SHADOW’s frequency extraction procedure results in 160 orbital harmonics for the 8.65d orbital period, 15 orbital harmonics for the 1.52d orbital period, 12 orbital harmonics for the 1.43d orbital period, and 884 other frequencies. These frequency lists form the basis of our subsequent asteroseismic analysis.

### 3.2. *period-spacing pattern identification*

The objective of this work is to provide asteroseismic analysis of the g-mode period-spacing pattern of KIC 4150611. This pattern is determined in Li et al. (2020a) to be the prograde dipole pattern. The low-frequency gravito-inertial modes detected in our target are often called prograde dipole modes, deriving from the limited notation  $(l, m) = (1, +1)$  in terms of spherical harmonics for reasons of simplicity; in reality this spherical harmonic component delivers only the dominant contribution to the actual Hough eigenfunction (Hough 1898) of such modes. For this reason, Lee & Saio (1997) introduced the more general notation  $(k, m) = (0, 1)$  for such modes, where  $k \equiv l - |m|$ .

We consider four different period-spacing patterns to evaluate how different extraction processes and pattern identification decisions can affect our results. The first pattern considered is the Li et al. (2020a) pattern, which we do not modify in any way. This pattern was also constructed from long-cadence *Kepler* data, but with a different light curve extraction and detrending process. A relatively low SNR threshold of 3 was applied

<sup>4</sup> <http://period04.net/>

<sup>5</sup> [https://github.com/LucIJspeert/star\\_shadow](https://github.com/LucIJspeert/star_shadow)



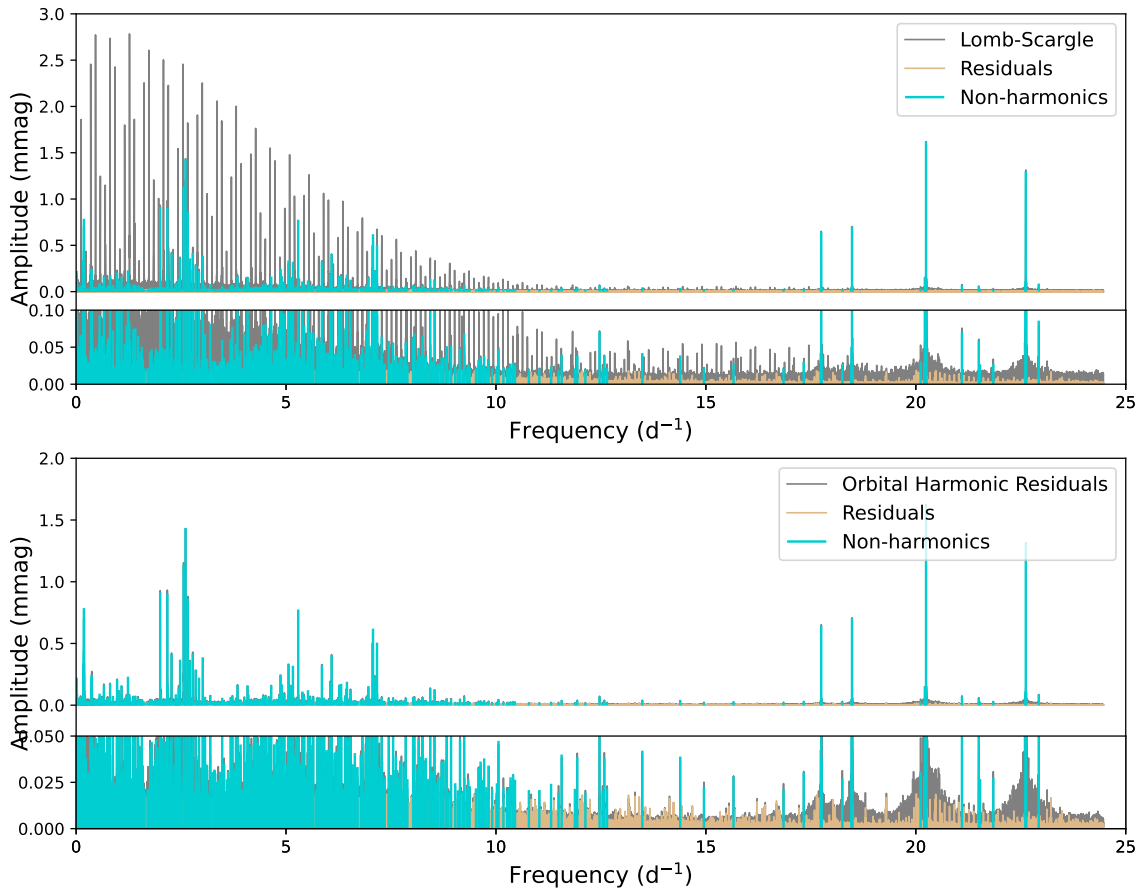


Fig. 4: Lomb-Scargle periodogram of the normalised, detrended light curve (grey) with non-orbital harmonic frequencies extracted by STAR SHADOW (light blue) and the periodogram of the residual light curve (orange). The lower panel is the periodogram of the light curve when the orbital harmonics (see Fig. 3) are removed.

when considering frequency significance by the algorithm employed by Li et al. (2020a). We will refer to this pattern as the PAT\_LI2020 pattern.

To construct period-spacing patterns from our own various light curves and their prewhitened frequency lists, we employ an iterative procedure relying on manually identifying candidate pattern members in the region of the Lomb-Scargle periodogram (Lomb 1976; Scargle 1982) relevant to  $\gamma$  Dor stars and (re-)fitting a theoretical asymptotic period-spacing pattern produced by AMiGO<sup>6</sup> (Van Reeth et al. 2016, 2018), which relies on the numerical approximations worked out by Townsend (2020).

AMiGO computes theoretical period-spacing patterns assuming a rigidly rotating, chemically homogeneous star under the traditional approximation of rotation (TAR, Eckart 1960; Berthomieu et al. 1978; Lee & Saio 1989, 1997; Mathis 2009; Bouabid et al. 2013; Van Reeth et al. 2016). Under the TAR, the horizontal component of the rotation vector is neglected, rendering the oscillation equations separable in spherical coordinates. The effect of rotation on the radial and azimuthal displacements are neglected while in the latitudinal direction they can be com-

puted by solving the Laplace tidal equation, for which solutions can be expressed in terms of Hough functions (Hough 1898). This achieves the accuracy required for the modelling of observed low-frequency modes in rotating stars, in contrast to perturbative asymptotic predictions (see, for example, Shibahashi 1979). Indeed, given the significant frequency shifts induced by the Coriolis acceleration (see, for example, Figures 3 & 4 in Aerts & Tkachenko 2024), one should not approximate gravito-inertial modes from computations in the perturbative regime.

The TAR is valid for modes where the displacement vector is dominant in the horizontal plane, which is an excellent approximation for  $\gamma$  Dor stars (Aerts 2021), including KIC 4150611. For the majority of these pulsators, the modes in the co-rotating frame have a frequency less than twice the rotation frequency, and the stellar rotation frequency is much less than both the Brunt-Väisälä and Lamb frequencies, which govern the stability of buoyant and acoustic restoring forces, respectively, to allow for mode propagation (Aerts & Tkachenko 2024). This allows for asymptotic period-spacing patterns to be computed as a function of the rotation frequency in the near-core region  $\Omega_c$  and the buoyancy travel time  $\Pi_0$  originally defined by Tassoul (1980):

<sup>6</sup> <https://github.com/TVanReeth/amigo>

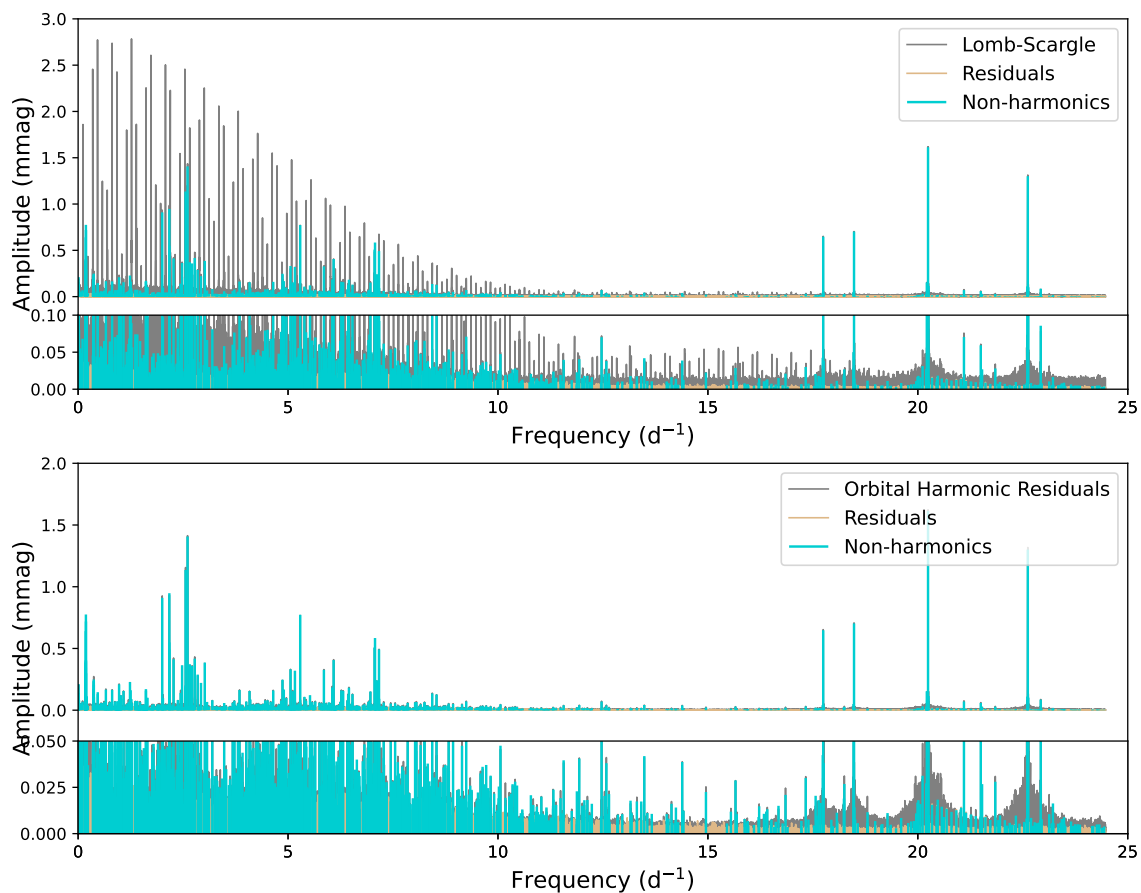


Fig. 5: As Fig. 4, but showing the period04 frequency extraction.

$$\Pi_0 = 2\pi^2 \left( \int_{r_1}^{r_2} N \frac{dr}{r} \right)^{-1}, \quad (1)$$

where  $N$  is the Brunt-Väisälä frequency and  $r_1$  and  $r_2$  are the boundaries of the mode cavity. The frequencies of the g-modes belonging to a period-spacing pattern of known degree  $l$  and azimuthal order  $m$  can then be computed according to:

$$f_{lmn} = \frac{\sqrt{\lambda_{lm,s}}}{(n + \alpha)\Pi_0} + m\Omega_c, \quad (2)$$

where  $\lambda_{lm,s}$  is the mode-specific eigenvalue of the Laplace tidal equation and  $\alpha$  is a phase term determined by the details of the mode-cavity boundaries, usually treated as a free parameter (around 0.5 in  $\gamma$  Dor stars) in practice (Bouabid et al. 2013; Van Reeth et al. 2015a, 2016). The value of  $\lambda_{lm,s}$  is determined for each oscillation frequency by its spin parameter  $s = 2\Omega_c/\omega_{lmn}$ , where  $\omega_{lmn}$  is the mode's angular frequency in the co-rotating reference frame.

AMiGO determines  $\lambda_{lm,s}$  using GYRE's 'lambda(nu)' function, first sampling a grid over a frequency domain appropriate to the star and then interpolating to determine precise values of

$\lambda_{lm,s}$  of each mode. In this way, AMiGO is able to quickly produce asymptotic period-spacing patterns for high-order gravito-inertial modes as a function of  $\Omega_c$  and  $\Pi_0$ .

By computing a grid of such patterns varying  $\Omega_c$  and  $\Pi_0$  and comparing with an observed period-spacing pattern, best-fitting values and uncertainty estimates for  $\Omega_c$  and  $\Pi_0$  can be obtained without computing detailed stellar and asteroseismic models. In addition to being faster, this has the advantage of avoiding unpredictable systematic errors due to uncertainty in the details of the input physics of stellar models. However, by the same token, the links between these predictions and the physics of stellar interiors is absent, limiting the inferences that can be drawn directly. Further, as a natural consequence of the underlying physical assumptions in the approach, structural information present in the pattern due to chemical gradients and other neglected physics cannot be reproduced. In stars where structural variations throughout the interior is large and induces deviations from a smooth period spacing pattern, the accuracy of the stellar parameters inferred of methods like AMiGO will be limited. This is not a concern in the case of KIC 4150611, where we observe a very smooth period-spacing pattern.

In addition to its utility in providing estimates of  $\Omega_c$  and  $\Pi_0$  (see Section 4.2), pattern predictions from theoretical frameworks such as AMiGO provide a useful aid in the identification

of oscillation frequencies that may form part of a period-spacing pattern, as highlighted by Van Reeth et al. (2015a). Starting from obvious pattern-members, we use AMiGO’s pattern predictions as a guide to assist in identifying additional candidate pattern oscillations, which we then feed back into AMiGO in an iterative process.

In this manner, we arrive at three period-spacing patterns (in addition to the previously identified pattern in Li et al. (2020a): two from the frequency list extracted using `period04` and one from the frequency list extracted using `STAR_SHADOW`. All patterns are included for ease of comparison in Fig. 6. The first pattern we obtain from the `period04` prewhitening process is extracted in a deliberately pessimistic manner, only taking frequencies that have SNR strictly above 5.6 (Baran et al. 2015) and are not ambiguous. The result is a pattern with several gaps and only short segments of consecutive modes, particularly at longer periods (equivalent to higher radial order  $n$ ). This pattern represents a pessimistic pattern selection, and we will refer to it as `PAT_P04_PES`.

The second pattern from the `period04` frequency list is obtained by selecting frequencies in a deliberately optimistic manner. In this selection, we allow moderate deviations below a SNR of 5.6, attempting to build the largest pattern possible. This includes judging whether a given mode is real and of stellar origin not only based on the mode’s own properties – such as its SNR – but also making use of prior knowledge of the existing pattern. The result is a more complete period-spacing pattern that extends to higher radial order modes than both the `PAT_LI2020` and `PAT_P04_PES` patterns. We refer to this pattern as `PAT_P04_OPT`.

The final pattern makes use of the `STAR_SHADOW` frequency list and is also obtained in an optimistic manner, allowing moderate deviations in SNR for modes which fit the rest of the pattern. The resulting pattern is similar in length and completeness to `PAT_P04_OPT`, although the different extraction procedure results in differences to the extraction of low amplitude, high-order modes relevant to the pattern. We refer to this pattern as `PAT_STS`.

Further details about the extraction characteristics in the period region surrounding `PAT_LI2020`, `PAT_P04_OPT`, `PAT_P04_PES` and `PAT_STS` are shown visually in Figs. A.1–A.4. The top panel of each figure shows the extracted frequencies, Lomb-Scargle periodogram for the relevant light curve with eclipse harmonics excluded, and the residual periodogram. The predicted frequencies from the AMiGO fit to the pattern are also shown, as well as the SNR and estimated errors in amplitude and period for each extracted mode. In Fig. A.1, the extracted frequencies, Lomb-Scargle periodogram, and residuals shown are from the `period04` frequency list for comparison with the `PAT_LI2020` period-spacing pattern, which is plotted along the x-axis. In all figures, the lower panels show the period-spacing pattern and relevant AMiGO fit to each pattern.

Note that while they are not shown in Figs. A.2–A.4, orbital harmonics, alias frequency predictions, and linear combinations of high-amplitude mode pairs were taken into account during pattern identification. Although there are several alias frequencies that fall within the domain of the period-spacing pattern, particularly those relating to the 94.2d orbit, none fall close enough to selected modes to be of concern.

There is a near-perfect coincidence between one of the 8.65d orbital harmonics and the extracted high-amplitude mode at 0.37d (this is excluded for this reason in the `PAT_P04_PES` pattern, but included in the `PAT_LI2020`, `PAT_P04_OPT`, and `PAT_STS` patterns). This is the cause of the nonphysical oscilla-

tory behaviour that appears in the 8.65d phase-fold when using the `period04` frequency list to construct harmonic models of the eclipses discussed in Kemp et al. (2024). This is avoided in the `STAR_SHADOW` extraction due to the enforcement of frequency-coupling between orbital harmonics. However, when comparing these patterns in Figure 6 (see also Fig. A.3 and A.4), it is clear that this makes little difference to the period-spacing pattern; the two patterns are essentially identical in the high-amplitude region below 0.4d.

All four patterns exhibit similar behaviour in the high-amplitude, short-period region. Differences only start to become noticeable when considering the low-amplitude, long-period modes. The `PAT_LI2020` period-spacing pattern’s second consecutive mode sequence (between approximately 0.4 and 0.43d) is very regular, but relies on extremely low-amplitude modes. Interestingly, it is the location of the second mode in this sequence – one of the relatively high SNR modes – that is the most noteworthy deviation when comparing with the `PAT_P04_OPT` and `PAT_STS` patterns. This mode is shifted slightly towards a lower period in both the `STAR_SHADOW` and `period04` frequency lists. The structure of the third consecutive sequence, between 0.43d and 0.46d, is essentially identical between all frequency lists.

`PAT_P04_PES`, `PAT_P04_OPT`, and `PAT_STS` all include modes beyond the third and final sequence of `PAT_LI2020`, although in the case of `PAT_P04_PES` this includes very few consecutive modes. Beyond the high amplitude peak at approximately 0.46d, there is a low amplitude valley followed by a high-amplitude peak. Several of these modes do not satisfy  $\text{SNR} > 5.6$ , and the predicted mode density in this region is approaching levels where chance coincidences of individual observed periods with the predicted would be a concern. Nonetheless, a series of modes with spacings consistent with the AMiGO predictions can be found here, noting that extracted frequencies in this region are different in places between the `PAT_STS` pattern and the `PAT_P04_OPT` pattern to the point where it appreciably affects the structure.

At this point, it is worth noting how the AMiGO fit predictions are used. Simply comparing the period predictions to the locations of extracted modes is often unhelpful, as individual oscillation periods can be affected by the chemical gradients inside the star. These period shifts manifest as structural glitches in the period-spacing pattern before quickly returning to the asymptotic behaviour, and are not able to be modelled by AMiGO. The structural glitch seen in the third consecutive sequence in `PAT_LI2020`, `PAT_P04_OPT`, and `PAT_STS` is an example of such a mode shift (around radial order 34 in Fig. 7).

It is clear that the inclusion – or not – of these high-order modes in the pattern has a much larger effect on the AMiGO fits than the differences in the actual mode frequencies between the different patterns. `PAT_LI2020` and `PAT_P04_PES` have relatively similar AMiGO fits, which rely far more upon the highest amplitude, short-period modes. Conversely, despite the structural differences between `PAT_P04_OPT` and `PAT_STS` at high radial orders, the fit between the two is near identical. As AMiGO only includes the physics needed for modelling the overall pattern shape, this is anticipated.

### 3.3. Asteroseismic grid modelling

The most expensive aspect of asteroseismic modelling using gravity modes is undoubtedly the computation of grids of stellar models and their pulsations. In order for the resolution of the grid not to adversely affect the results, dense stellar grids are required. These grids must, at minimum, span the zero-age main

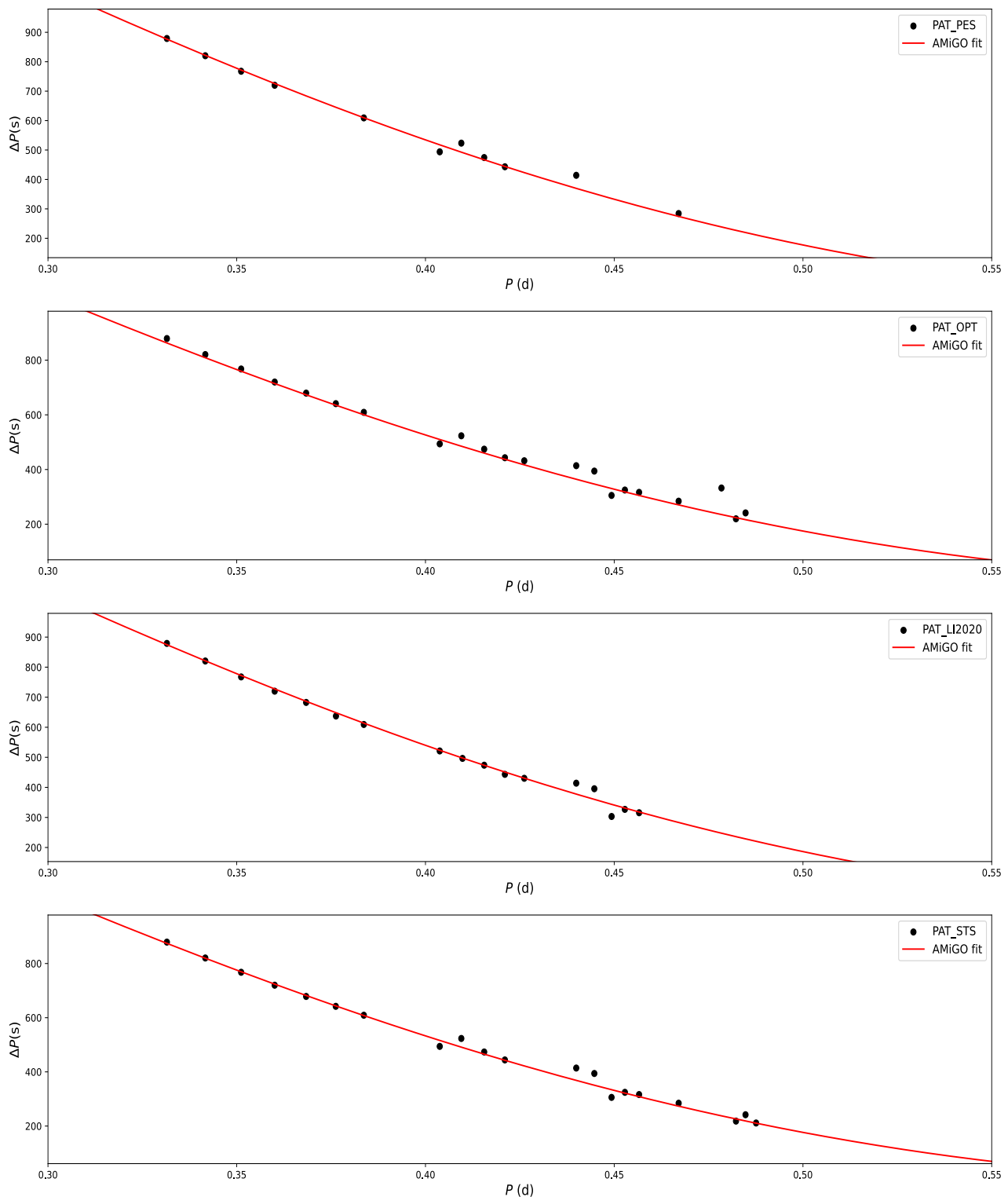


Fig. 6: period-spacing patterns considered in this work, along with their AMiGO fits.

sequence (ZAMS) mass and an age proxy such as the central hydrogen mass fraction,  $X_c$ . As the tilt of a period-spacing pattern is highly sensitive to the near-core rotation frequency  $\Omega_c$ , dense sampling of this parameter is required when computing the pulsations if the pattern is to be compared with directly. The required sampling density of  $\Omega_c$  can be reduced by optimising the rotation scaling independently as part of the merit function, essentially finding the most probable  $\Omega_c$  for each structural model

(see Michielsen et al. 2023). However, probing other additional stellar physics such as convective boundary mixing parameters (e.g., the degree of step (Shaviv & Salpeter 1973; Zahn 1991) or exponential (Freytag et al. 1996; Herwig 2000) overshooting) each involve adding another dimension to a grid of stellar models that multiplies the computational cost.

Table 1: External constraints and labelling conventions

Label	$T_{\text{eff}}$ (K)	$\log(g)$ (dex)	$R$ ( $R_{\odot}$ )
All	-	-	-
Spectro	7130-7430	3.84-4.44	-
R	-	-	1.55-1.75
R and Spectro	7130-7430	3.84-4.44	1.55-1.75
Tight R	-	-	1.63-1.65
Tight R and Spectro	7130-7430	3.84-4.44	-

**Notes.** The default external constraints are formed by doubling the error estimates from Kemp et al. (2024). The ‘Tight R’ constraint is closer to the formal  $1-\sigma$  uncertainty under a spectroscopically constrained light fraction (see Kemp et al. 2024 for details).

In this work, we make use of C-3PO<sup>7</sup>, a neural network-driven asteroseismic modelling code for  $\gamma$  Dor stars (Mombarg et al. 2021). It rapidly makes predictions for the pulsation frequencies, period-spacings, and radial-orders of a star based on its mass  $M$ ,  $X_{\text{c}}$ , metallicity  $Z$ ,  $\Omega_{\text{c}}$ , and degree of exponential core overshooting  $f_{\text{ov}}$ . This is accomplished by taking the average frequency prediction from five different neural networks dedicated to this task. A separate neural network computes  $T_{\text{eff}}$  and  $\log(g)$ , common physical constraints from spectroscopy, while another computes the luminosity  $L$  for each model, which can then be compared with astrometric luminosities such as those from *Gaia* (Gaia Collaboration et al. 2016). The underlying stellar structure and pulsation models used to train C-3PO were computed using MESA (Paxton et al. 2013) and GYRE (Townsend & Teitler 2013) respectively. Despite not including rotation explicitly, the training set used for C-3PO used stellar models computed with a constant envelope mixing ( $D_{\text{mix}} = 1 \text{ cm}^2 \text{ s}^{-1}$ ) to account for transport processes in the envelope. This low level of  $D_{\text{mix}}$  reflects the low levels of envelope mixing found in  $\gamma$  Dor stars (Van Reeth et al. 2016; Mombarg et al. 2019). The training set includes a diffusive-exponential core overshoot prescription, varying the diffusive exponential overshoot factor  $f_{\text{ov}}$  between 0.01-0.03. The training set spans the  $\gamma$  Dor range in mass ( $1.3 M_{\odot}$ – $2.0 M_{\odot}$ ) and spans a small range of metallicities around solar ( $Z=0.011$ - $0.015$ ). Further details of the underlying physics of the MESA models and GYRE pulsation models on which the network is trained can be found in Mombarg et al. (2021).

In addition to the neural network predictor modules, C-3PO includes a modelling framework that handles both radial-order matching using the neural-network’s pulsation predictions and assigning merit values for each model. The period-spacing patterns are built by matching the first period in the longest sequence of consecutive modes, and building out the pattern to the other sequences from there. The merit function includes both the periods and the period spacings; this can be viewed as a compromise between constraining power and sensitivity to un-modelled physics. Michielsen et al. (2021) find that, for their case-study star of KIC 7760680, a slowly pulsating B (SPB) star with an exceptionally long period-spacing pattern with a high level of structure, a merit function accounting only for the periods is inferior to one accounting only for mode period spacings, citing high variance in theoretical mode predictions for the pulsation periods. By combining both period-spacings and periods, C-3PO’s methodology attempts to ensure that period-spacings are accurately fit, while rewarding models that also have agreement in the mode periods.

Michielsen et al. (2021) also compare two merit functions: the commonly used  $\chi^2$  and the Mahalanobis distance (MD, Johnson et al. 2019) with an additional term for the model variance (Aerts et al. 2018). This additional term adjusts the weight given to each observation according to both the degree of covariance between each observable according to the model grid – in this way attempting to measure the modelling uncertainty – on top of the covariance between the observables themselves. This results in a broadening of the parameter-space, widening uncertainty regions. Michielsen et al. (2021) find that the MD-based merit function outperforms the  $\chi^2$  merit function insofar as it arrives at more realistic uncertainties. However, an important caveat is that KIC 7760680 had an unusually long and complete period-spacing pattern with prominent structures that could be mostly explained by physics included within the underlying pulsation models.

Preliminary analysis on KIC 4150611 making use of the forward modelling software package Foam (Michielsen 2024) revealed that use of the MD-based merit function led to poor fits to the period-spacing pattern regardless of whether the period-spacing or the periods were fit. Patterns which vaguely approximated the structural glitches in the period-spacing pattern strongly preferred despite those models utterly failing to reproduce the rest of the pattern. The  $\chi^2$  statistic, on the other hand, placed no special weight on those structures, instead favouring patterns which matched the observed pattern as a whole.

C-3PO supports both the  $\chi^2$  and the MD-based merit function merit functions; we make use of the  $\chi^2$  for KIC 4150611. C-3PO’s modelling framework also supports using external constraints such as  $T_{\text{eff}}$ ,  $\log(g)$ , and  $L$  in the sampling phase, which can allow for more efficient sampling of the relevant space. We do not make use of this feature, instead opting to compute many models uniformly distributed across the entire  $\gamma$  Dor range. This is to facilitate discussion of the relative constraining power of asteroseismic, spectroscopic, and eclipse-modelling observables and their combinations for different stellar parameters. To assess the impact of sampling effects on our results, we compute our results using two different samples for each pattern: a medium resolution sample, with  $8 \times 10^5$  models across the  $\gamma$  Dor range, and a high resolution sample, with  $3 \times 10^6$  models. We present the results from the high resolution sampling in the main text, while the results from the alternative ‘Tight R’ radius constraint in the appendices. All figures relating to the medium resolution sampling are included in the online supplementary material. A summary of the different configurations of external constraints considered is presented in Table 1.

We provide an estimate of the uncertainty for our C-3PO modelling by estimating a  $1 - \sigma$   $\chi^2$  cut-off using equation 9 from Mombarg et al. (2021), and then taking the maximum and minimum parameter values from that distribution to form the  $1 - \sigma$  estimate. These uncertainty estimates should be treated with caution, particularly for cases where the parameters do not have normal (or even quasi-normal)  $\chi^2$  envelopes. Further, the  $1 - \sigma$  sub-samples these margins are based on contain relatively few (20-40) models in the most constraining case, adding an element of stochasticity to their estimation.

### 3.4. MCMC parameter-based grid-search.

To better understand the correlations between and the uncertainty structure of our parameter estimates, we also employed a classical MCMC grid search. This was done using several different grids of stellar models (grids A-E):

<sup>7</sup> <https://github.com/JMombarg/c3po>



- Grid A: a grid composed of the lowest metallicity non-rotating models from Mombarg et al. (2021) (the same underlying models used to train C-3P0).
- Grid B: a grid composed of solar-metallicity, rotating stellar models from Mombarg et al. (2024a) (employing hydrodynamic envelope mixing and angular momentum transport based on the rotation, as well as microscopic diffusion).
- Grid C: a grid of rotating solar metallicity models from Mombarg et al. (2024b) (employing rotational mixing but with fixed viscosity and no microscopic diffusion).
- Grid D: a grid of  $Z=0.0045$  models also from Mombarg et al. (2024b).
- Grid E: a grid of  $Z=0.008$  models with physics equivalent to Mombarg et al. (2024b) (Aerts et al. 2024).

Note that although the grid of low-metallicity models from Mombarg et al. (2021) is from the same set used to train C-3P0, it is considerably denser, as C-3P0 was trained only on the subset of stellar models where GYRE pulsation models were computed.

The grid search employed an MCMC sampling method similar to Fritzewski et al. (2024) based on the external constraints  $T_{\text{eff}}$ ,  $R$ ,  $L$ ,  $\log g$ , and the asteroseismic measurement of the buoyancy travel time parameter  $\Pi_0$ . For the rotating stellar models, the asteroseismic near-core rotation  $\Omega_c$  was also used. We allowed the MCMC walkers to explore the grid in three unconstrained parameters  $M$ ,  $f_{\text{ov}}$ , and  $X_c$  while keeping the envelope mixing fixed to  $D_{\text{mix}} = 1 \text{ cm}^2 \text{ s}^{-1}$ . We assumed a flat prior for all parameters.

## 4. Results

In this section, we present the results of our asteroseismic modelling of the g-mode period-spacing pattern of KIC 4150611 Aa.

### 4.1. Pattern fits

The best-fitting models to the relevant period-spacing patterns that satisfy the radius and spectroscopic constraints are included in Fig. 7. These best-fitting models fit the overall shape and location of the periods and period-spacing patterns satisfactorily, and subtle structural features in the observed patterns are able to be modelled in many cases. The fact that the fits make no effort to model the stronger dips and features in the observed patterns is reassuring, as it implies a level of resilience of the methodology to un-modelled physics or badly extracted frequencies (the two are functionally identical and often indistinguishable from a modelling perspective). The quality of the fits, including the apathy towards the larger structural features, is very similar when considering the best overall asteroseismic fit without considering external constraints, as opposed to the best constrained fit shown in Fig. 7.

An interesting example of the models' ability to reproduce the small-scale structure is the fit to the PAT\_LI2020 pattern from radial orders 25-29 in Fig. 7a. The structure here is only slight, but is able to be reproduced very well by the model. What makes this segment particularly interesting is that the same structure reappears in the fits to the other period-spacing patterns, which include a glitch around the spacings of the 25th and 26th radial order modes. This implies that this structure is an inevitable consequence of matching other parts of the pattern well, most likely the robust first segment (radial orders 16-22). This in turn leads to the conclusion that, at least for this segment, the

PAT\_LI2020 pattern is most likely the correct accurate extraction despite our inability to reproduce its structure in any of the other three patterns.

In contrast, the structure of the third segment (the spacings of radial orders 32-36) is consistent between all three patterns where it was able to be extracted (PAT\_LI2020, PAT\_P04\_OPT, and PAT\_STS). In all three cases, it is dominated by a large glitch that is not reproduced by our current models.

Beyond this sequence, only the PAT\_P04\_OPT and PAT\_STS patterns are worth discussing, as PAT\_LI2020 does not extract beyond the third sequence and PAT\_P04\_PES extracts only the spacing for the 39th radial order mode. Both PAT\_P04\_OPT and PAT\_STS include four consecutive modes at high radial order, although the modes extracted differ between the two patterns: PAT\_P04\_OPT includes spacings for the radial orders 43-45, while PAT\_STS includes the spacings of radial orders 44-46. The common radial orders between both patterns,  $n = 44$  and  $n = 45$ , are in agreement and reproduced by their models. However, while the  $n = 46$  mode is reproduced by the model fitting the PAT\_STS pattern, the  $n = 43$  mode in the PAT\_P04\_OPT pattern is not. Considering its low amplitude, we consider its detection spurious.

### 4.2. Parameter estimates

Figs. 8-11 show the results of the parameter estimation component of our modelling work when considering our default case of conservative external constraints. The upper triangular panels present heat maps (dark being better fitting) tracking the maximum of the  $1/\chi^2$  merit function considering all samples, irrespective of external constraints. The panels on the main diagonal present distributions and envelopes of the  $1/\chi^2$  merit function for each parameter, as well as the best-fitting models when considering different external constraints (see Table 1). Finally, the lower triangular panels are 'scatter-pies'<sup>8</sup> showing how the different external constraints (see Table 1) manifest in each 2D projection of the landscape, with the best-fitting models for each external constraint also shown. Further guidance on reading these figures can be found in the figure caption of Fig. 8, and the parameters of the best fitting models for each pattern and each external constraint are tabulated in Table 2.

Before we delve deeper into each parameter, it is informative to make a few general comments about the results obtained for each pattern. The first thing to note is that the best-fitting model for the PAT\_P04\_OPT and PAT\_STS patterns, while different between each pattern, is the same when considering the asteroseismology in an unconstrained manner and when considering both the radius and spectroscopic constraints. This is not the case for the PAT\_LI2020 and PAT\_P04\_PES patterns; in the PAT\_LI2020 pattern, the best fitting asteroseismic solution satisfies the spectroscopic constraint but not the radius constraint, while for the PAT\_P04\_PES pattern, the best fitting asteroseismic solution does not satisfy any of the external constraints. Although this could be coincidence, this can be easily understood by considering that the PAT\_P04\_OPT and PAT\_STS patterns contain the most identified spacings, and are therefore more constraining than the shorter PAT\_LI2020 and PAT\_P04\_PES patterns.

<sup>8</sup> Equivalent to 2-D histogram, but rather than colouring by the count instead a pie chart is drawn in each bin accounting for the relative number of qualitatively different data (here the different combinations of external constraints). Code for producing scatter-pies can be found at: <https://github.com/Alex162/scatterpie>

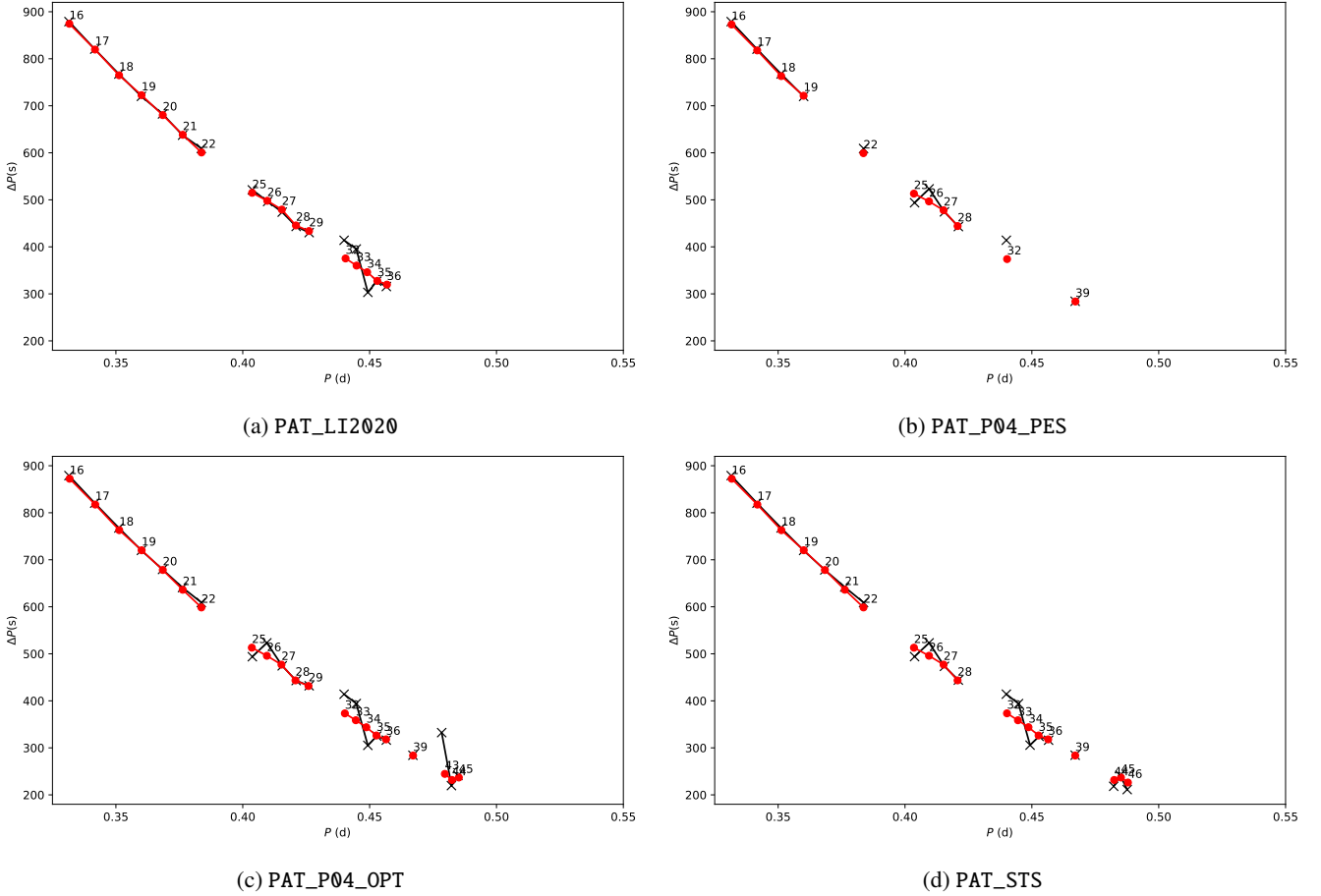


Fig. 7: Best-fitting C-3PO models (red) consistent with the radial and spectroscopic constraints (see Table 2). Observed patterns are shown in black.

The other general comment to be made is that in every case, the best-fitting model from the subset that satisfies the relevant radius constraint (either the tight constraint or the more conservative default constraint) also satisfies the spectroscopic constraints on  $T_{\text{eff}}$  and  $\log(g)$ . This is in spite of the fact that, as can be seen from the lower triangular panels of Figs. 8-11, for many parameters the radius and spectroscopic external constraints have near-orthogonal intersections.

We will now discuss each parameter, beginning with those for which calculations can be made without relying on grids of stellar models ( $\Omega_c$  and  $\Pi_0$ ), followed by the model-dependent parameters that are directly obtained from the modelling framework ( $M$ ,  $X_c$ ,  $Z$ ,  $f_{\text{ov}}$ ,  $T_{\text{eff}}$ ,  $\log(g)$ , and  $\log(L)$ ) and finally the stellar age, which we estimate from the underlying training sets, and the stellar radius, which we calculate for each model using the stellar mass and its surface gravity.

#### 4.2.1. Near-core rotation frequency

As previously explained, the near-core rotation frequency and buoyancy travel time can be directly obtained from the period-spacing patterns without comparison with detailed stellar pulsation models by using a purely theoretical framework. Under the assumptions described in Section 3.2, theoretical patterns depending on  $\Omega_c$  and  $\Pi_0$  were computed using AMiGO and fit to the observed period-spacing pattern, providing both best-fitting values and an uncertainty estimate for these two parameters. The

best-fitting asymptotic patterns to each observed period-spacing pattern can be found in Fig. 6 and the lower panels of Figs. A.1-A.4. For the PAT\_LI2020 pattern, we obtain an estimate for the near-core rotation rate of  $\Omega_c = 1.562 \pm 0.016 \text{ d}^{-1}$ , while the other three patterns give estimates of approximately  $1.577 \pm 0.010 \text{ d}^{-1}$ . These results are consistent with the  $1.58 \pm 0.01 \text{ d}^{-1}$  estimate from Li et al. (2020a).

Previously, in Section 2, we estimated the surface rotation frequency for Aa using the radius and radial velocity estimates from Kemp et al. (2024) to be  $\Omega_{\text{surf}} = 1.54 \pm 0.10 \text{ d}^{-1}$ . Using our  $\Omega_c$  estimate of  $1.58 \pm 0.01$ , we can conservatively estimate the surface-to-core rotation fraction as:  $\Omega_{\text{surf}} / \Omega_c = 0.975 \pm 0.064$ . This is consistent with the picture of quasi-rigid core-to-surface rotation presented in Fig. 6 of Aerts (2021) for main sequence F-type stars. Aa's  $\Omega_c$  of approximately  $1.58 \text{ d}^{-1}$  ( $18 \mu\text{Hz}$ ) and  $\log(g)$  of  $4.14 \pm 0.18$  (Kemp et al. 2024) place it in the middle of the well-populated clump of other rapidly rotating F-type stars.

As a final comment, we note that it is possible to relax the assumption of rigid rotation, and instead consider a theoretical asymptotic pattern accounting for slightly radially-differential rotation within the star (Ogilvie & Lin 2004; Mathis et al. 2008; Mathis 2009; Van Reeth et al. 2018). However, inferring differential rotation in stellar interiors in this way requires either rotational mode-splittings on top of a period-spacing pattern (e.g., as in Triana et al. 2015; Schmid & Aerts 2016) or the characterisation of multiple period-spacing patterns within the star to break the degeneracy with rigid rotation (Van Reeth et al. 2018). In Van Reeth et al. (2018), it was concluded that for all but the

Table 2: Parameters of the best-fitting models from C-3PO’s high resolution sample for each pattern under different external constraints.

Pattern	Sample	$M$	$X_c$	$R$	$f_{ov}$	$Z$	$\log(T_{\text{eff}})$	$\log(g)$	$\log(L)$
		$M_{\odot}$	-	$R_{\odot}$	-	-	dex	dex	dex
PAT_LI2020	All	$1.958^{+0.02}_{-0.622}$	$0.07^{+0.625}_{-0.018}$	$3.051^{+0.86}_{-1.793}$	$0.011^{+0.004}_{-0.0}$	$0.01^{+0.019}_{-0.0}$	$3.8554^{+0.0}_{-0.062}$	$3.7612^{+0.6032}_{-0.2299}$	$1.343^{+0.0295}_{-0.8698}$
PAT_LI2020	Spectro	$1.958^{+0.02}_{-0.566}$	$0.07^{+0.569}_{-0.017}$	$3.051^{+0.164}_{-1.698}$	$0.011^{+0.003}_{-0.0}$	$0.01^{+0.005}_{-0.0}$	$3.8554^{+0.0}_{-0.0109}$	$3.7612^{+0.5581}_{-0.0432}$	$1.343^{+0.0216}_{-0.7621}$
PAT_LI2020	R	$1.478^{+0.042}_{-0.1}$	$0.471^{+0.013}_{-0.09}$	$1.589^{+0.16}_{-0.038}$	$0.011^{+0.004}_{-0.0}$	$0.011^{+0.015}_{-0.0}$	$3.8537^{+0.0009}_{-0.0241}$	$4.2057^{+0.0113}_{-0.0979}$	$0.7629^{+0.0752}_{-0.0782}$
PAT_LI2020	R and Spectro	$1.478^{+0.042}_{-0.035}$	$0.471^{+0.013}_{-0.084}$	$1.589^{+0.158}_{-0.038}$	$0.011^{+0.003}_{-0.0}$	$0.011^{+0.004}_{-0.0}$	$3.8537^{+0.0009}_{-0.0088}$	$4.2057^{+0.0113}_{-0.0788}$	$0.7629^{+0.0752}_{-0.0391}$
PAT_LI2020	Tight R	$1.459^{+0.061}_{-0.081}$	$0.424^{+0.06}_{-0.043}$	$1.644^{+0.104}_{-0.093}$	$0.014^{+0.001}_{-0.003}$	$0.011^{+0.015}_{-0.0}$	$3.8466^{+0.0079}_{-0.017}$	$4.1703^{+0.0467}_{-0.0624}$	$0.7656^{+0.0725}_{-0.0809}$
PAT_LI2020	Tight R and Spectro	$1.459^{+0.061}_{-0.016}$	$0.424^{+0.06}_{-0.037}$	$1.644^{+0.103}_{-0.093}$	$0.014^{+0.0}_{-0.003}$	$0.011^{+0.004}_{-0.0}$	$3.8466^{+0.0079}_{-0.0018}$	$4.1703^{+0.0467}_{-0.0434}$	$0.7656^{+0.0725}_{-0.0418}$
PAT_P04_PES	All	$1.693^{+0.297}_{-0.367}$	$0.185^{+0.512}_{-0.132}$	$2.375^{+1.014}_{-1.099}$	$0.013^{+0.002}_{-0.002}$	$0.01^{+0.009}_{-0.0}$	$3.8434^{+0.0112}_{-0.019}$	$3.9158^{+0.4379}_{-0.25}$	$1.0765^{+0.2985}_{-0.5963}$
PAT_P04_PES	Spectro	$1.471^{+0.519}_{-0.091}$	$0.495^{+0.149}_{-0.436}$	$1.553^{+1.612}_{-0.212}$	$0.011^{+0.004}_{-0.0}$	$0.01^{+0.005}_{-0.0}$	$3.8544^{+0.0002}_{-0.0099}$	$4.2234^{+0.1}_{-0.4869}$	$0.7447^{+0.6304}_{-0.1775}$
PAT_P04_PES	R	$1.471^{+0.05}_{-0.04}$	$0.495^{+0.0}_{-0.098}$	$1.553^{+0.175}_{-0.003}$	$0.011^{+0.004}_{-0.0}$	$0.01^{+0.006}_{-0.0}$	$3.8544^{+0.0002}_{-0.0126}$	$4.2234^{+0.0}_{-0.0857}$	$0.7447^{+0.0927}_{-0.0363}$
PAT_P04_PES	R and Spectro	$1.471^{+0.05}_{-0.032}$	$0.495^{+0.0}_{-0.098}$	$1.553^{+0.175}_{-0.003}$	$0.011^{+0.004}_{-0.0}$	$0.01^{+0.005}_{-0.0}$	$3.8544^{+0.0002}_{-0.0084}$	$4.2234^{+0.0}_{-0.0781}$	$0.7447^{+0.0927}_{-0.0194}$
PAT_P04_PES	Tight R	$1.494^{+0.027}_{-0.063}$	$0.437^{+0.058}_{-0.04}$	$1.65^{+0.078}_{-0.1}$	$0.011^{+0.004}_{-0.0}$	$0.011^{+0.005}_{-0.001}$	$3.8546^{+0.0}_{-0.0128}$	$4.1778^{+0.0456}_{-0.04}$	$0.7952^{+0.0421}_{-0.0869}$
PAT_P04_PES	Tight R and Spectro	$1.494^{+0.027}_{-0.055}$	$0.437^{+0.058}_{-0.04}$	$1.65^{+0.078}_{-0.1}$	$0.011^{+0.004}_{-0.0}$	$0.011^{+0.003}_{-0.001}$	$3.8546^{+0.0}_{-0.0086}$	$4.1778^{+0.0456}_{-0.0325}$	$0.7952^{+0.0421}_{-0.07}$
PAT_P04_OPT	All	$1.512^{+0.487}_{-0.187}$	$0.424^{+0.275}_{-0.374}$	$1.678^{+2.586}_{-0.43}$	$0.011^{+0.004}_{-0.0}$	$0.01^{+0.02}_{-0.0}$	$3.8558^{+0.0086}_{-0.0639}$	$4.1681^{+0.1995}_{-0.6915}$	$0.8188^{+0.6574}_{-0.3604}$
PAT_P04_OPT	Spectro	$1.512^{+0.477}_{-0.127}$	$0.424^{+0.273}_{-0.368}$	$1.678^{+1.689}_{-0.363}$	$0.011^{+0.004}_{-0.0}$	$0.01^{+0.02}_{-0.0}$	$3.8558^{+0.0086}_{-0.0115}$	$4.1681^{+0.1762}_{-0.488}$	$0.8188^{+0.5865}_{-0.259}$
PAT_P04_OPT	R	$1.512^{+0.047}_{-0.094}$	$0.424^{+0.125}_{-0.053}$	$1.678^{+0.069}_{-0.126}$	$0.011^{+0.004}_{-0.0}$	$0.01^{+0.02}_{-0.0}$	$3.8558^{+0.0086}_{-0.0147}$	$4.1681^{+0.0591}_{-0.0481}$	$0.8188^{+0.059}_{-0.1058}$
PAT_P04_OPT	R and Spectro	$1.512^{+0.047}_{-0.071}$	$0.424^{+0.125}_{-0.055}$	$1.678^{+0.069}_{-0.126}$	$0.011^{+0.004}_{-0.0}$	$0.01^{+0.02}_{-0.0}$	$3.8558^{+0.0086}_{-0.011}$	$4.1681^{+0.0591}_{-0.0405}$	$0.8188^{+0.059}_{-0.0873}$
PAT_P04_OPT	Tight R	$1.492^{+0.067}_{-0.074}$	$0.441^{+0.108}_{-0.07}$	$1.639^{+0.109}_{-0.086}$	$0.012^{+0.003}_{-0.001}$	$0.01^{+0.02}_{-0.0}$	$3.8556^{+0.0089}_{-0.0145}$	$4.1831^{+0.0441}_{-0.0631}$	$0.7925^{+0.0853}_{-0.0795}$
PAT_P04_OPT	Tight R and Spectro	$1.492^{+0.067}_{-0.051}$	$0.441^{+0.108}_{-0.051}$	$1.639^{+0.109}_{-0.086}$	$0.012^{+0.003}_{-0.001}$	$0.01^{+0.02}_{-0.0}$	$3.8556^{+0.0089}_{-0.0108}$	$4.1831^{+0.0441}_{-0.0555}$	$0.7925^{+0.0853}_{-0.061}$
PAT_STS	All	$1.506^{+0.491}_{-0.164}$	$0.434^{+0.26}_{-0.376}$	$1.659^{+1.544}_{-0.394}$	$0.011^{+0.004}_{-0.0}$	$0.01^{+0.005}_{-0.0}$	$3.8561^{+0.0023}_{-0.0252}$	$4.1764^{+0.1851}_{-0.4517}$	$0.8087^{+0.5706}_{-0.3264}$
PAT_STS	Spectro	$1.506^{+0.491}_{-0.129}$	$0.434^{+0.235}_{-0.376}$	$1.659^{+1.544}_{-0.342}$	$0.011^{+0.004}_{-0.0}$	$0.01^{+0.004}_{-0.0}$	$3.8561^{+0.0023}_{-0.0118}$	$4.1764^{+0.1617}_{-0.4503}$	$0.8087^{+0.5706}_{-0.2635}$
PAT_STS	R	$1.506^{+0.0}_{-0.075}$	$0.434^{+0.034}_{-0.045}$	$1.659^{+0.068}_{-0.09}$	$0.011^{+0.004}_{-0.0}$	$0.01^{+0.004}_{-0.0}$	$3.8561^{+0.0}_{-0.0137}$	$4.1764^{+0.03}_{-0.0443}$	$0.8087^{+0.0062}_{-0.0825}$
<b>PAT_STS</b>	<b>R and Spectro</b>	<b><math>1.506^{+0.0}_{-0.071}</math></b>	<b><math>0.434^{+0.034}_{-0.045}</math></b>	<b><math>1.659^{+0.068}_{-0.09}</math></b>	<b><math>0.011^{+0.004}_{-0.0}</math></b>	<b><math>0.01^{+0.004}_{-0.0}</math></b>	<b><math>3.8561^{+0.0}_{-0.0116}</math></b>	<b><math>4.1764^{+0.03}_{-0.0443}</math></b>	<b><math>0.8087^{+0.0062}_{-0.0807}</math></b>
PAT_STS	Tight R	$1.455^{+0.051}_{-0.024}$	$0.434^{+0.034}_{-0.045}$	$1.632^{+0.094}_{-0.063}$	$0.014^{+0.001}_{-0.003}$	$0.012^{+0.003}_{-0.001}$	$3.8463^{+0.0098}_{-0.0039}$	$4.1756^{+0.0308}_{-0.0434}$	$0.7589^{+0.056}_{-0.0327}$
PAT_STS	Tight R and Spectro	$1.455^{+0.051}_{-0.02}$	$0.434^{+0.034}_{-0.045}$	$1.632^{+0.094}_{-0.063}$	$0.014^{+0.001}_{-0.003}$	$0.012^{+0.003}_{-0.001}$	$3.8463^{+0.0098}_{-0.0018}$	$4.1756^{+0.0308}_{-0.0434}$	$0.7589^{+0.056}_{-0.0309}$

**Notes.** The externally constrained PAT\_STS pattern is the preferred solution, and marked in bold. The units of  $T_{\text{eff}}$ ,  $g$ , and  $L$  are K,  $\text{g cm}^{-3}$ , and  $L_{\odot}$ . The sub-samples are described in Table 1.

most extreme cases of differential rotation, only stars exhibiting period-spacing patterns in both prograde-dipole and Rossby modes have sufficient distinguishing power to unravel differential from rigid rotation. In KIC 4150611, we identified neither rotational mode splitting – even in the high-amplitude p-modes – nor a reliable<sup>9</sup> additional period-spacing pattern, precluding further conclusions of the level of differential core-to-envelope rotation other than to say that the rotation is rigid within the measurement errors when comparing the asteroseismic near-core rotation and the surface rotation derived from spectroscopy.

#### 4.2.2. Buoyancy travel time

Similarly to  $\Omega_c$ , the buoyancy travel time  $\Pi_0$  can be estimated directly from AMiGo’s fit to the pattern using the TAR (see Section 3.2). For all patterns except the PAT\_LI2020 pattern, AMiGo estimates  $\Pi_0$  to be approximately  $4024 \pm 74$  s; for the PAT\_LI2020 pattern, similarly to  $\Omega_c$ , a slightly lower  $\Pi_0$  with a higher uncertainty is obtained ( $\Pi_0 = 3941 \pm 112$  s). These estimates are consistent with the  $\Pi_0$  estimate of  $4050 \pm 80$  s from Li et al. (2020b). We return to the question of the stellar age later, but if Aa was

<sup>9</sup> In Appendix C we discuss the possibility of a very short  $l = 2$  series of g-modes.

very young (as suggested by Helminiak et al. 2017’s isochrone fitting) we would expect a significantly higher  $\Pi_0$  ( $\Pi_0 > 4400$  s).

#### 4.2.3. Stellar mass

Due to the importance of stellar mass in determining so much of stellar evolution, it is of particular interest to obtain an estimate. Obtaining a precise constraint is difficult in  $\gamma$  Dor stars due to degeneracies with  $X_c$  and  $Z$  (Mombarg et al. 2019). There is indeed significant variation in this parameter when considering the best-fitting models for each pattern and the different external constraints (see Table 2).

Considering first the pure asteroseismology, (the ‘All’ case, where all models are considered), we can see that the envelope for the stellar mass is quite flat for all patterns, implying poor constraining power. This is reflected in the uncertainty estimates, which span the entire  $\gamma$  Dor region. Considering only the best-fitting values, the less constraining PAT\_LI2020 and PAT\_P04\_PES patterns arrive at best-fitting models with relatively high mass,  $1.96 M_{\odot}$  and  $1.69 M_{\odot}$  respectively. The more constraining PAT\_P04\_OPT and PAT\_STS models arrive at lower mass best-fitting models, at  $1.506 M_{\odot}$  and  $1.512 M_{\odot}$  respectively. It is clear from the envelopes that obtaining a confident mass es-

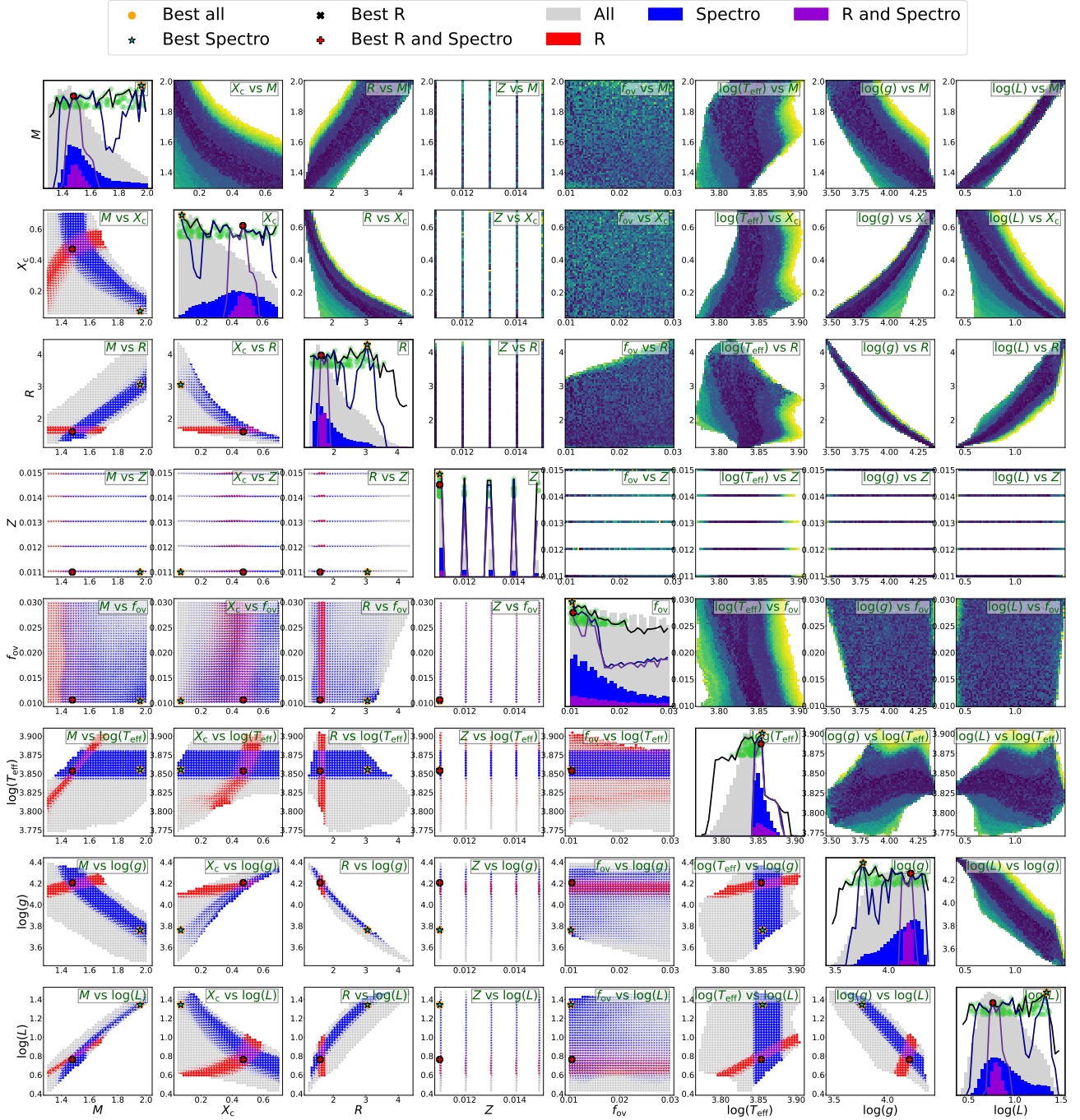


Fig. 8: PAT\_LI2020 modelling results. The main diagonal (emphasised with thicker panel outlines) shows the  $1/\chi^2$  envelopes (the maximum value of  $1/\chi^2$  per bin, solid lines) and histograms of the  $1/\chi^2$  values for each variable along the x-axis when considering purely the asteroseismic fit (All, grey), when only considering models that fall within spectroscopic constraints on  $\log(g)$  and  $T_{\text{eff}}$  (Spectro, blue), and when considering only models that satisfy both the spectroscopic constraints and constraints on the stellar radius from eclipse modelling (R and Spectro, purple). Best fitting models are shown for each case. The green markers indicate the 100 best-fitting models. The lower triangular panels are ‘scatter-pies’ (see main text) showing how the different external constraints intersect along each 2D projection of the parameter space, with the best-fitting models also shown. The upper triangular panels show the maximum value of  $1/\chi^2$  for each 2D bin (logarithmic scale, with dark colouration indicating a better fit).

imate from asteroseismic observables alone for KIC 4150611 is impossible even for the longer period-spacing patterns.

Examining the lower triangular panels of Figs. 8-11, it is clear that in isolation the radius and spectroscopic constraints each provide little information on the mass, with each spanning most of the considered parameter-space. When considered together, however, a near-orthogonal intersecting region is pro-

duced that, even with our conservative ( $2\text{-}\sigma$ ) constraints on the stellar radius,  $T_{\text{eff}}$ , and  $\log(g)$ , constrains the stellar mass to between 1.4 and 1.6  $M_{\odot}$ . Enforcing the tight radius constraint ( $1.64 \pm 0.01 R_{\odot}$ ) offers only a slight improvement.

When considering all observables together, the best-fitting models for all period-spacing patterns have masses between 1.47 and 1.51  $M_{\odot}$ , with PAT\_LI2020 and PAT\_P04\_PES favouring a



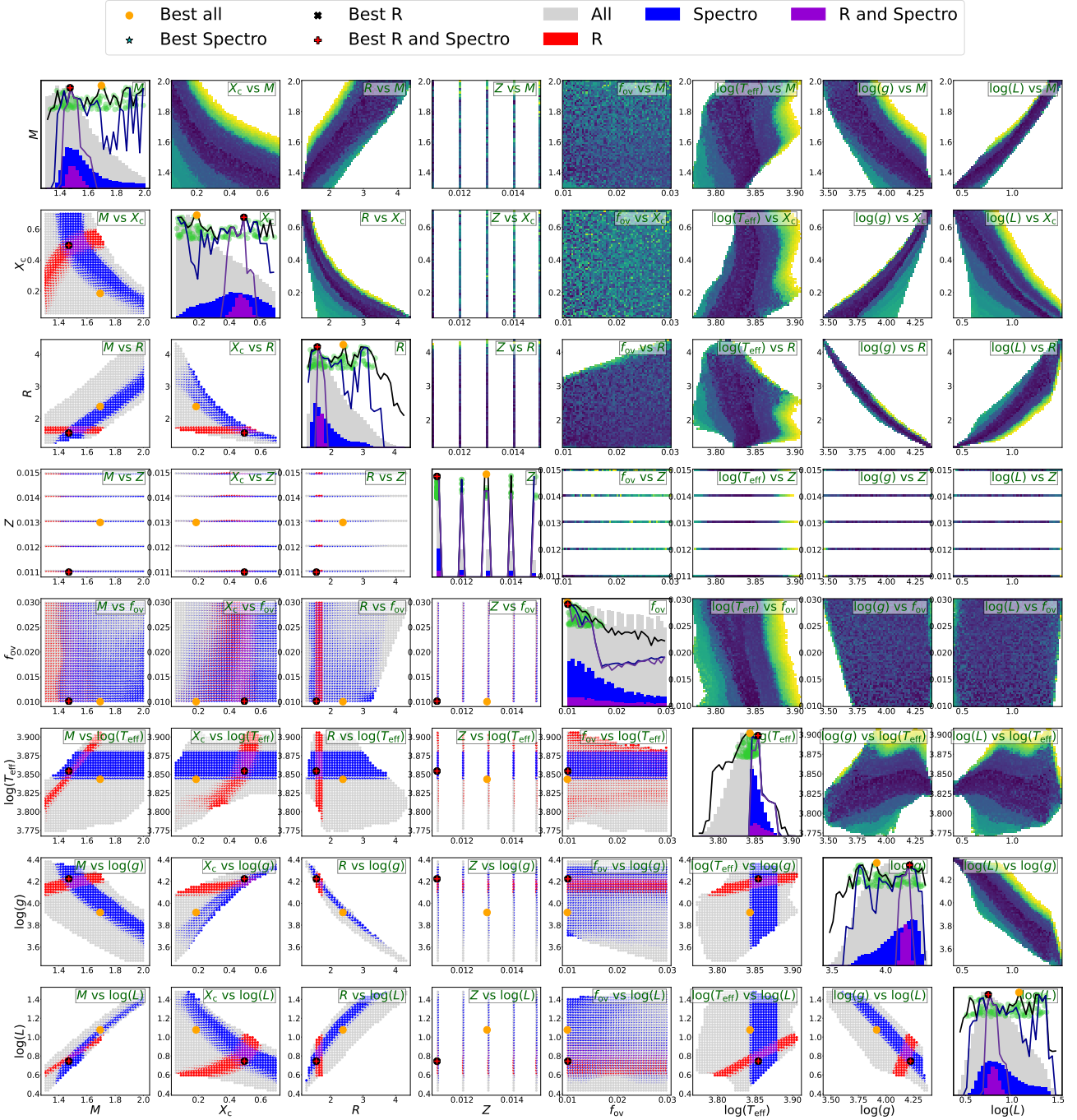


Fig. 9: PAT\_P04\_PES modelling results.

lower mass estimate around  $1.47\text{--}1.48 M_{\odot}$  and PAT\_P04\_OPT and PAT\_STS favouring a slightly higher mass around  $1.50\text{--}1.51 M_{\odot}$ . The medium resolution sampling arrives at very similar results:  $1.46\text{--}1.51 M_{\odot}$ , and the same bifurcation between the PAT\_LI2020/PAT\_P04\_PES and PAT\_P04\_OPT/PAT\_STS patterns. Typical  $1 - \sigma$  error estimates are approximately  $\pm 0.05 M_{\odot}$  when considering only the sub-sample of models satisfying the external constraints. Enforcing a tight radius constraint changes little, with the various patterns still arriving at best-fitting stellar models with stellar masses between  $1.47$  and  $1.50 M_{\odot}$ , while the bifurcation between the PAT\_LI2020/PAT\_P04\_PES and PAT\_P04\_OPT/PAT\_STS solutions disappears. Considering the variation in the best-fitting models, we arrive at a precision of better than 2% in mass.

#### 4.2.4. Core hydrogen fraction

The core hydrogen fraction is a proxy for the stellar age, a property of particular interest for KIC 4150611. Helminiak et al. (2017) estimate the age of the B binary (two G stars) to be approximately 35 Myr from isochrone fitting. Considering the large number of eclipses in an otherwise uncrowded field and the tentative dynamical association between the A triple and the B binary (Helminiak et al. 2017), the co-evolution assumption is quite well motivated for KIC 4150611. Under this assumption, an asteroseismic estimate of  $X_c$  parameter can be used to put this previous age to the test. A 35 Myr age for KIC 4150611 would imply that Aa is the youngest  $\gamma$  Dor star observed to date. We



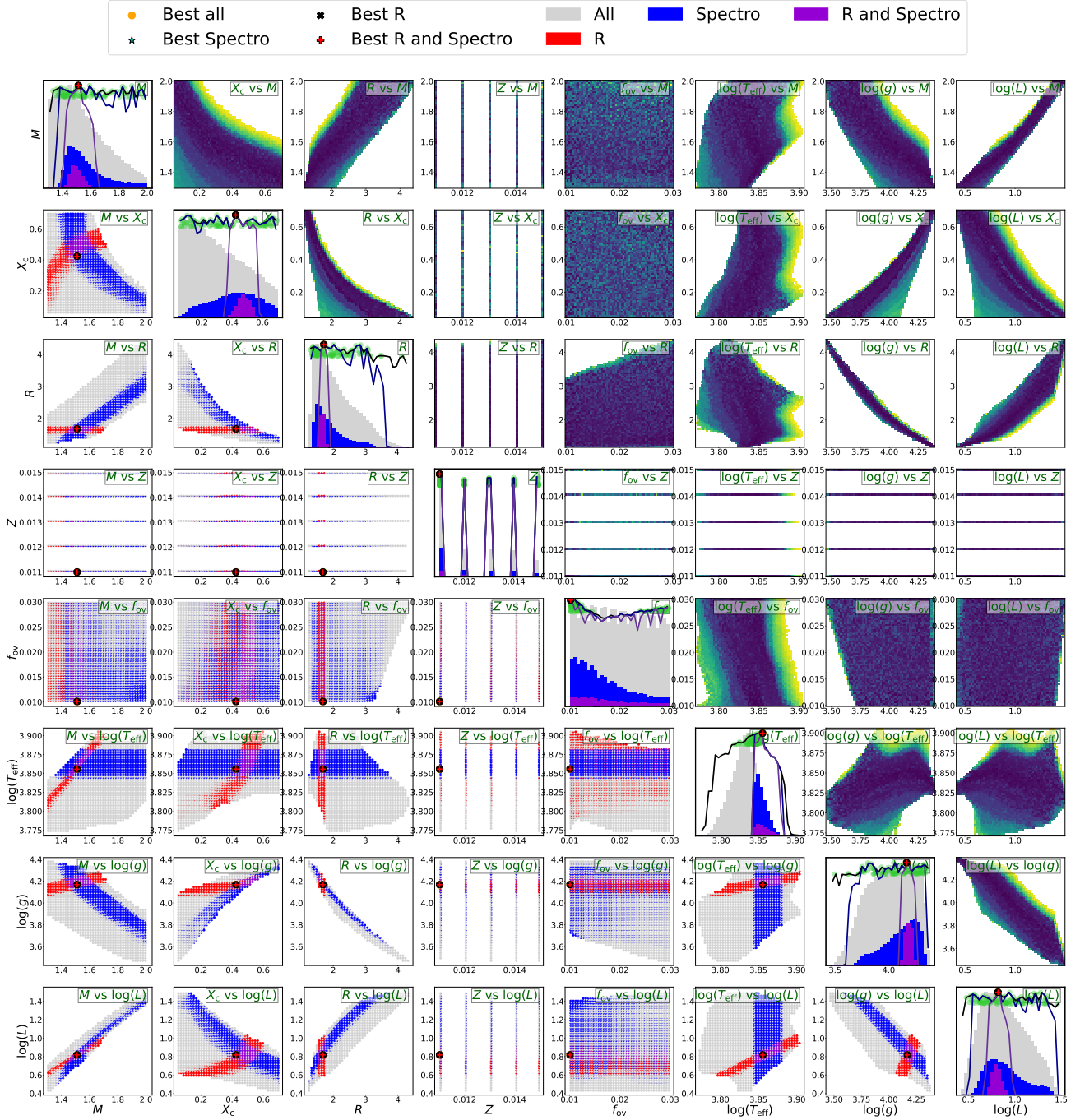


Fig. 10: PAT\_P04\_OPT modelling results

will return to the stellar age after concluding our discussion on C-3PO's directly modelled parameters.

Firstly, it is important to note that the stellar mass and  $X_c$  are highly correlated in the asteroseismic fits, reflected in the strong banding present in the 2D envelope seen in the upper triangular panels showing  $X_c$  vs  $M$  in Figs. 8-11. For this reason, much of the previous discussion surrounding  $M$  is relevant to  $X_c$ .

Once again first considering the pure asteroseismic estimations, due to the correlated nature of  $X_c$  and  $M$  the high mass estimates of the PAT\_LI2020 and PAT\_P04\_PES patterns translate to low estimates of  $X_c$ , with the converse true for the PAT\_P04\_OPT and PAT\_STS patterns. Further, we note that once again the envelope is mostly flat, and therefore poorly constrain-

ing, with the  $1-\sigma$  error estimate once again spanning almost the entire range of possible values of  $X_c$  (0-0.7).

Considering the external spectroscopic and eclipse modelling constraints without the benefit of asteroseismology, a fairly broad bounding constraint between 0.38 and 0.58 in  $X_c$  can be placed<sup>10</sup>.

Considering the external constraints and the asteroseismology in conjunction, we see that the best-fitting models have  $X_c$  varying between 0.42 and 0.49 from the high resolution sampling, with PAT\_LI2020 and PAT\_P04\_PES favouring higher  $X_c$  and PAT\_P04\_OPT and PAT\_STS favouring lower  $X_c$ , as expected

<sup>10</sup> The initial core hydrogen fraction is approximately 0.7, with the precise value depending on the metallicity

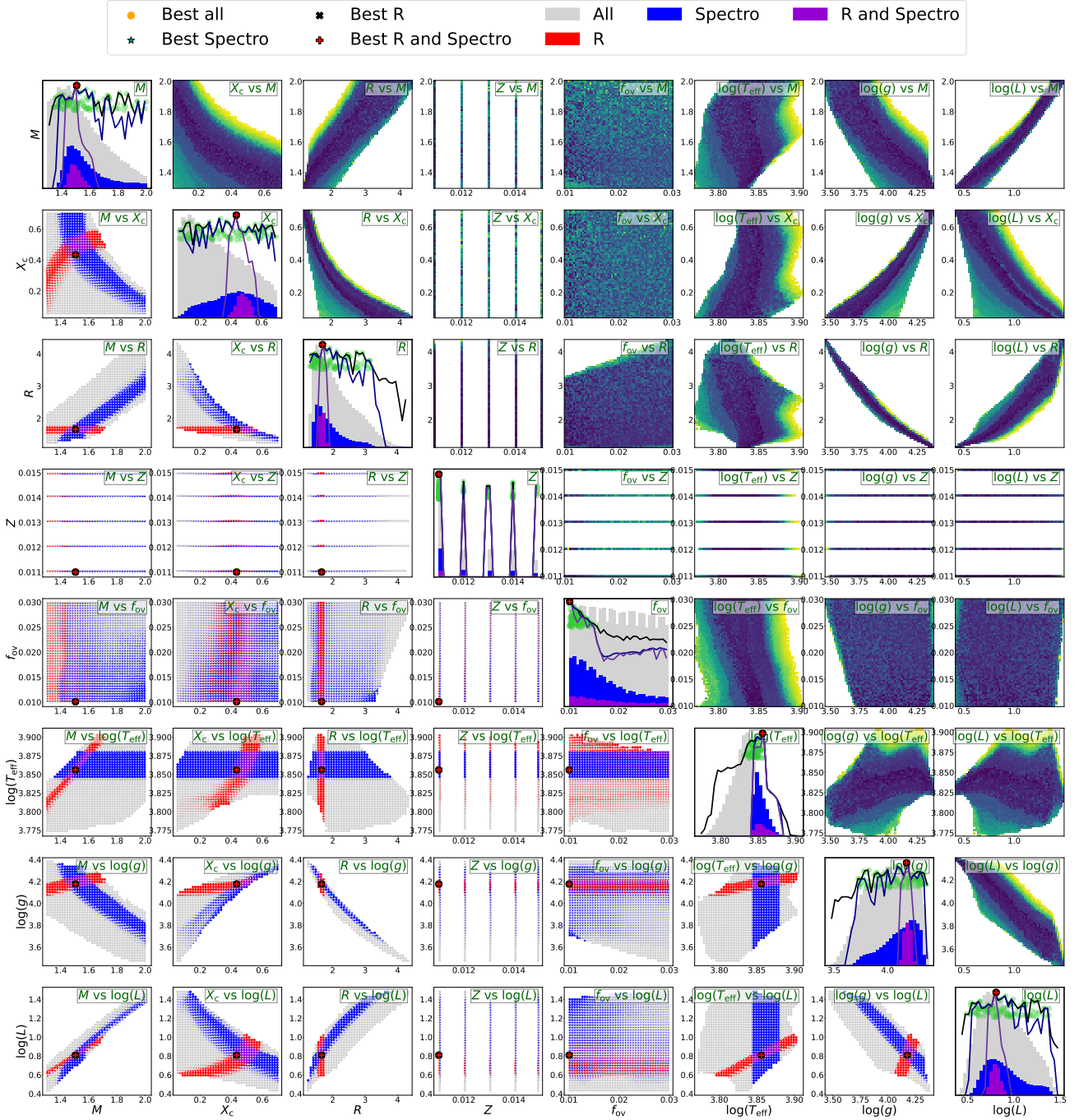


Fig. 11: PAT\_STS modelling results

given their preferences towards a higher stellar mass estimate. Estimated  $1 - \sigma$  uncertainties for these constrained values are at most  $\pm 0.1$ , and appear to be significantly lower for some patterns ( $\pm 0.04$  in the case of PAT\_STS, for example). Enforcing the tight radius constraint results in best values for  $X_c$  between 0.42 and 0.44.

#### 4.2.5. Metallicity

The sampling in  $Z$  is low resolution, with only 5 different cases able to be considered over a narrow range ( $Z=0.011-0.015$ ). There does, however, seem to be a preference towards lower metallicity solutions, especially when the radius and spectro-

scopic constraints are taken into consideration, although the envelope is very flat.

From atmospheric analysis of the disentangled spectrum of Aa in Kemp et al. (2024), we have a metallicity estimate of  $[M/H] = -0.23 \pm 0.06$ , corresponding to  $Z = 0.0084 \pm 0.0011$  (using the solar metallicity of  $Z_{\odot} = 0.0142857$  from Asplund et al. 2009, following Mombarg et al. 2021). This places the star in the middle of the metallicity range of  $\gamma$  Dor stars with metallicity measurements from high-resolution spectroscopy (Gebauer et al. 2021). This metallicity is slightly outside the bounds of the training set for C-3P0, which has a lower limit of 0.011. Armed with the knowledge of the spectroscopic metallicity measurement, we note that the preference towards lower metallicity could imply a small degree of sensitivity to  $Z$  in the asteroseismic

fits. However, precise estimation of metallicity from g-modes in isolation is unlikely to be possible in practise due to degeneracy between the stellar mass and metallicity.

#### 4.2.6. Exponential overshooting factor

The exponential overshooting factor determines the degree of exponential core overshooting in the core boundary region. Mombarg et al. (2021) vary this from between 0.01 and 0.03 to form their training set.

For all patterns except PAT\_P04\_OPT, which has a (very flat) ‘U’ distribution spanning the full range of  $f_{ov}$ , there is a clear preference towards low exponential overshooting. This is consistent with the empirical  $M$ - $f_{ov}$  relation of Claret & Torres (2017), who found values of  $f_{ov}$  between 0.005 and 0.02 across the  $\gamma$  Dor range, with lower values associated with the low-mass end regime 1.4-1.5  $M_{\odot}$ . We note that Mombarg et al. (2024a) find no such correlation between the stellar mass and  $f_{ov}$ , but do find that low values of  $f_{ov}$  are most probable in  $\gamma$  Dor stars.

Despite the fact that  $f_{ov}$  can affect the stellar radius and other external properties such as the luminosity, we find that the radius and spectroscopic constraints provide no useful constraint on this parameter either when considered in isolation or their intersection.

#### 4.2.7. Effective temperature and surface gravity

From atmospheric analysis on the disentangled spectra using GSSP (Tkachenko 2015), we have an estimate for the effective temperature and surface gravity of  $T_{eff}=7280 \pm 70$  K ( $\log(T_{eff})=3.8621 \pm 0.0042$  dex) and  $\log(g)=4.14 \pm 0.18$  dex.

A centrally peaked envelope around (approximately) the spectroscopic solution is present with or without external considerations for all patterns, although the PAT\_P04\_OPT pattern’s envelope is significantly flatter and broader. The best-fitting  $\log(T_{eff})$  solutions – excluding the extreme case of  $\log(T_{eff})=3.843$  dex for the PAT\_P04\_PES pattern considered without external constraints – vary from between 3.855-3.856 dex, placing them slightly below the lower bound of the  $1-\sigma$  uncertainty of the GSSP estimate. Considering that the effective temperature was not part of the merit function, this level of agreement is quite good, although we note that the best-fitting models for all patterns slightly under-predict the spectroscopic solution. Uncertainty estimates for the upper limit of  $\log(T_{eff})$  can be as high as +0.008 dex, and are even larger when considering lower temperatures (approximately  $-0.012$  dex). These uncertainties are sufficiently large that they overlap with the spectroscopic estimate for  $T_{eff}$ .

Spectroscopy only places loose constraints on  $\log(g)$  ( $\log(g)=4.14 \pm 0.18$  dex, Kemp et al. 2024), with the  $2-\sigma$  uncertainty region essentially spanning the entire  $\gamma$  Dor range. However, the radius constraint from the eclipse modelling narrows the viable region considerably. Combining the spectroscopic and radius constraints allows bounding constraints to be placed on  $\log(g)$  of 4.15-4.25 dex, consistent with the spectroscopic solution. Within this far smaller region, the envelope of the asteroseismic merit function is peaked, although the best-fitting solution still varies significantly from pattern to pattern. PAT\_LI2020 and PAT\_P04\_PES arrive at higher estimates for  $\log(g)$ , 4.206 dex and 4.223 dex, respectively, while the best fitting solutions for PAT\_P04\_OPT and PAT\_STS arrive at  $\log(g)$  of 4.168 dex and 4.176 dex, respectively. For all patterns, a slightly higher  $\log(g)$  than the face value of the spectroscopic solution is

preferred, although all three cases are, as a result of the already constraining intersection between the radius and spectroscopic solutions, well within the spectroscopic  $1-\sigma$  uncertainty region. Typical  $1-\sigma$  uncertainties of the constrained asteroseismic modelling are estimated to be approximately  $\pm 0.04$  dex.

#### 4.2.8. Luminosity

The luminosity  $\chi^2$  envelope is, similarly to  $\log(g)$ , characterised by a broad and relatively flat envelope when considering the asteroseismology in isolation. The spectroscopic constraints affect this little, although it is interesting to note that, when looking at the histogram of the asteroseismic merit function, the peak roughly coincides with the region consistent with the intersection between the spectroscopic and radius constraints.

Also similarly to  $\log(g)$ , imposing both the spectroscopic and radius constraints allows bounding constraints to be placed on  $\log(L)$  (0.7-0.9 dex). PAT\_LI2020 and PAT\_P04\_PES arrive at lower estimates for  $\log(L)$  of 0.763 dex and 0.745 dex respectively, while the best fitting solutions for PAT\_P04\_OPT and PAT\_STS arrive at estimates for  $\log(L)$  of 0.819 dex and 0.809 dex respectively. Estimated  $1-\sigma$  uncertainties are approximately +0.006 and  $-0.003$  for the externally constrained asteroseismic solutions.

From *Gaia* DR3, we have  $\log(L)$  estimates for Aa of  $\log(L) = 0.804 \pm 0.017$  dex assuming a light fraction of 0.82, and  $\log(L) = 0.838 \pm 0.017$  dex assuming a light fraction of 0.92 (see Section 2). Considering our best-fitting solutions, the lower values of the PAT\_LI2020 and PAT\_P04\_PES solutions for  $\log(L)$  (0.763 dex and 0.745 dex respectively) are closer to, but still underestimate, even the lower light fraction (0.85) luminosity estimate preferred by the eclipse modelling and Helminiak et al. (2017). The higher values of  $\log(L)$  implied by the best-fitting solutions of the PAT\_P04\_OPT and PAT\_STS patterns (0.819 dex and 0.809 dex), however, are consistent with the *Gaia* luminosity regardless of which light fraction is assumed.

#### 4.2.9. Stellar age

The stellar age can be estimated from the mass and core hydrogen fraction, although there are secondary physical influences such as birth composition, rotation, and degree of core-envelope mixing. The stellar age is not directly predicted by C-3PO, but an estimate can be obtained by searching within the C-3PO training set for the nearest model in terms of  $M$ ,  $Z$ , and  $f_{ov}$ , where mass is prioritised, and then interpolating the age from the evolution history using  $X_c$ . The resolution within the training set is too poor for any useful inference of most other stellar properties, but the dominant dependence on  $M$  and  $X_c$  makes this technique viable for the stellar age. We provide tabulated information on the nearest training model for each solution in the online supplementary material, but caution against using it to infer other stellar properties.

Doing so results in stellar age estimates of 830 Myr, 1230 Myr, 1100 Myr, and 1070 Myr for the PAT\_LI2020, PAT\_P04\_PES, PAT\_P04\_OPT, and PAT\_STS patterns respectively for the pure asteroseismic best-fitting solutions. The externally constrained solutions have age estimates of 1280, 1200, 1100, and 1070 Myr for the PAT\_LI2020, PAT\_P04\_PES, PAT\_P04\_OPT, and PAT\_STS patterns, respectively.

This is clearly inconsistent with the very young 35 Myr age estimate for the B binary from Helminiak et al. (2017). Such a young age would require a very high  $X_c$  estimate for any star

within the  $\gamma$  Dor range; even a  $2 M_{\odot}$  star has a main sequence lifetime of almost a 1000 Myr.

As previously discussed, the external constraints – which are quite conservative – impose a maximum value for  $X_c$  of 0.58 when considering their intersection, already resulting in stellar ages significantly older than 35 Myr. Considering the asteroseismology in isolation, there is little evidence of a peak at very high  $X_c$  when considering the envelope, and none when external constraints are considered. Further, the buoyancy travel time is too low for the star to be so young. The approximately 100 Myr-old  $\gamma$  Dor stars in NGC 2516 have buoyancy travel times of around 4800 s (Li et al. 2024), for example, and these may be the youngest  $\gamma$  Dor stars aged to date.

In Kemp et al. (2024), radius and mass ratio estimates were obtained not only for the primary pulsator Aa, but also the members of the tight Ab eclipsing binary, composed of two K/M dwarfs. The radius estimates for these two dwarf stars were significantly smaller than the radii implied by Helminiak et al. (2017)’s isochrone fits to the B binary, which placed these stars on the pre-main sequence. Their smaller size, therefore, implies older stars have already contracted to the zero-age main sequence. Kemp et al. (2024) noted that this could imply that the co-evolution assumption between the A triple and the B binary could be invalid, but could also simply be due to the large inherent uncertainty associated with isochrone fits. The Helminiak et al. (2017) isochrone fit for Aa, a  $1.64 M_{\odot}$  star with a radius of only  $1.376 R_{\odot}$ , was also significantly different than the approximately  $1.65 R_{\odot}$  radius estimate from the eclipse modelling, which could also imply an older star. Considering all of this information, we consider an age estimate of  $1100 \pm 100$  Myr to be a robust update on the previous isochrone-based age estimate.

#### 4.2.10. Stellar radius

The stellar radius of Aa and its uncertainty is dealt with in detail in Kemp et al. (2024), and forms one of the external constraints. Here, we discuss the ability of the asteroseismic and spectroscopic observables to estimate the stellar radius and the level of agreement between the modelling work and the radius estimate from Kemp et al. (2024).

Considering the asteroseismology in conjunction with the spectroscopic constraints, a bimodal envelope pattern structure appears, with one broad peak at low stellar radius (consistent with the eclipse radius) and a second at high radius (around  $3 R_{\odot}$ ). This feature is present (although varies in prominence) in all four considered patterns.

Considering the level of consistency with the radius estimate from Kemp et al. (2024), the best-fitting asteroseismic models with radius and spectroscopic external constraints applied have radii of 1.59, 1.55, 1.68, and  $1.66 R_{\odot}$  for the PAT\_LI2020, PAT\_P04\_PES, PAT\_P04\_OPT, and PAT\_STS patterns respectively in the high-resolution sampling. The  $1-\sigma$  uncertainties are estimated to be as high as  $\pm 0.1 R_{\odot}$ , with the lower PAT\_LI2020 and PAT\_P04\_PES estimates being skewed towards higher radius estimates. Kemp et al. (2024) considered the effect of variation in the light-fraction of Aa, finding  $R_{Aa} = 1.65 \pm 0.01 R_{\odot}$ ,  $R_{Aa} = 1.62 \pm 0.01 R_{\odot}$ , and  $R_{Aa} = 1.61 \pm 0.02 R_{\odot}$ , for the 0.92-0.96, 0.83-0.87, and ‘free’ light fraction cases respectively. On the basis of their spectroscopic analysis, Kemp et al. (2024) preferred the 0.92-0.96 light fraction solution. In the context of our asteroseismic modelling, all three of Kemp et al. (2024)’s radius estimates are so similar that it would be a stretch to say one is preferred. We do note, however, that the more constraining asteroseismic patterns, PAT\_P04\_OPT and PAT\_STS, both arrive at

best-fitting values of the stellar radius ( $1.68 R_{\odot}$  and  $1.66 R_{\odot}$ ) that are consistent with the radius estimates from the eclipse modelling.

#### 4.3. MCMC grid search

Five different grids of stellar models (grids A-E, see section 3.4) were considered for as part of the MCMC parameter-based grid-search. All MCMC simulations converged to a solution, but not all solutions were able to recover all input parameters satisfactorily, implying that a consistent model did not exist within the grid. Grids A (a  $Z=0.011$ , non-rotating grid from Mombarg et al. (2021)), C (a solar metallicity, rotating grid from Mombarg et al. (2024b)), and E (a  $Z=0.008$ , rotating grid with equivalent physics to Mombarg et al. (2024b)) were able to recover all input parameters, and we will discuss their solutions later in this section. Grids B (a solar metallicity, rotating grid from Mombarg et al. (2024a) including hydrodynamic rotational mixing) and D (a  $Z=0.0045$ , rotating grid from Mombarg et al. (2024b)) were not able to recover the input parameters.

Grid B has the most sophisticated stellar physics treatment for stellar mixing; however, its computation at solar metallicity poses an issue. Figure 12 shows the large effect that metallicity has on the crucial asteroseismic parameter  $\Pi_0$ , on which the ageing of the star chiefly depends. Comparing grids A and B, we found the effect of metallicity on the buoyancy travel time was at least several hundred seconds, compared to only a few tens of seconds from the rotation. The metallicity of KIC 4150611 is determined spectroscopically to be  $Z = 0.0084$ , significantly lower than the  $Z \approx 0.014$  solar metallicity adopted in Mombarg et al. (2021, 2024a). This miss-match in metallicity may be responsible for the inability of the MCMC simulation using grid B to find a solution consistent with all observables.

However, the treatment of mixing can also affect  $\Pi_0$  significantly; the solar metallicity models from Mombarg et al. (2024b) (grid C) have a similar  $\Pi_0$  profile to the  $Z = 0.011$  profile in Figure 12 (grid A), differing significantly from the solar metallicity models of Mombarg et al. (2024a) (grid B). This implies that internal physical choices can be as important as matching the metallicity when using  $\Pi_0$ . The  $Z = 0.0045$  (grid D) models from Mombarg et al. (2024b) have significantly lower values of  $\Pi_0$ , as anticipated, but also a very flat  $\Pi_0$ - $X_c$  behaviour between  $X_c = 0.55$  and  $X_c = 0.3$ , implying lower sensitivity to stellar ages in this region. This flattening is particularly pronounced for higher  $f_{ov}$ .

Considering now only the MCMC simulations where the input parameters were able to be recovered within uncertainty (grids A, C, and E), we find that the results are broadly consistent with the pattern modelling approach using C-3PO and consistent with each-other. We also note that, as we might expect, grid E – which most closely matches the metallicity of KIC 4150611 – does a slightly better job at recovering the input parameters.

From our MCMC modelling, we estimate KIC 4150611 to be a  $1.52 \pm 0.06 M_{\odot}$  star with  $X_c = 0.48 \pm 0.08$ , values consistent with those found by our C-3PO modelling, albeit slightly higher in the case of  $X_c = 0.48 \pm 0.08$ . This methodology was unable to constrain  $f_{ov}$ , likely due to this parameter being insufficiently constrained by  $\Pi_0$  alone. This was also the case in Fritzewski et al. (2024), and highlights the added value of pattern-modelling relative to parameter-based grid search methods.

However, one advantage of the MCMC method is its ability to sample all evolutionary parameters accessible through the MCMC chain, giving access to stellar properties that cannot be directly accessed via C-3PO. We estimate the stellar age to



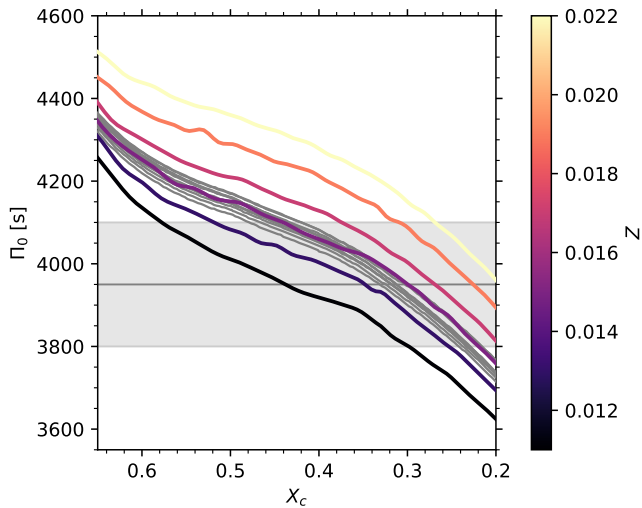


Fig. 12: Buoyancy travel time vs central H fraction for a  $1.5 M_{\odot}$  star, for various metallicities, using data from Mombarg et al. (2021). The buoyancy travel time for KIC 4150611 (see Section 4, which is an input for the MCMC grid-search component of the modelling, is shown as the horizontal grey band. The grey lines are the solar metallicity, rotating stellar models from Mombarg et al. (2024a) (grid B); the width of the band that they form is indicative of the variation due to stellar rotation.

be  $1110 \pm 150$  Myr, in agreement with our previous estimates. Further, we find a convective core mass fraction  $M_{\text{conv}}/M = 0.09 \pm 0.01$ , which is consistent with the distribution of other *Kepler*  $\gamma$  Dor stars (Mombarg et al. 2019).

## 5. Conclusions

In this work, we modelled the gravity-mode period-spacing pattern of the Aa component of KIC 4150611 with the goal of estimating its stellar parameters. This was done with attention to how the different external constraints from spectroscopy and photometric eclipse modelling interplay with the asteroseismic information. We also considered four different period-spacing patterns for the system to account for systematic differences in pattern identification and frequency extraction methods.

We find that pattern-dependent frequency variations are less important than the completeness of the pattern, particularly in terms of how far the pattern extends to high radial orders. In several key parameters, such as the stellar mass and core hydrogen fraction, there is a clear bifurcation between the parameter estimation from the shorter patterns, PAT\_LI2020 and PAT\_P04\_PES, and the longer PAT\_P04\_OPT and PAT\_STS patterns. The parameters for the longer PAT\_P04\_OPT and particularly the PAT\_STS patterns agree best with external information from the eclipse modelling, spectroscopy, and the system luminosity calculated from *Gaia* DR3 data.

For patterns of similar length and completeness to KIC 4150611, the pattern may not be constraining enough for confident conclusions to be drawn for many stellar parameters without the benefit of external constraints. Notable exceptions include near-core properties such as the degree of exponential overshoot and the near-core rotation. The effective temperature also appears to be able to be consistently estimated from the seismology alone, likely due to it being correlated with the buoyancy travel time.

When the external spectroscopic and constraints are considered in isolation, they are generally uninformative for any given parameter. However, the intersection of their  $2\text{-}\sigma$  uncertainty regions does allow for useful – although imprecise – bounds to be placed on the mass, central hydrogen fraction, and luminosity. However, it is unhelpful when considering the metallicity, degree of core overshooting, and the near-core rotation.

We find the near-core rotation rate to be  $1.58 \pm 0.01 \text{ d}^{-1}$ , consistent with Li et al. (2020a). Combined with an estimate for the surface rotation frequency of  $1.54 \pm 0.10 \text{ d}^{-1}$ , this is consistent with near-perfect rigid rotation of the radiative zone. We also estimate the buoyancy travel time to be  $4024 \pm 74 \text{ s}$ , also consistent with Li et al. (2020a).

Considering the intersection of the  $2\text{-}\sigma$  uncertainty regions of the spectroscopic and constraints in conjunction with the asteroseismology, we arrive at the best motivated constraints of the stellar parameters. The stellar mass we estimate to be between  $1.47 M_{\odot}$  and  $1.51 M_{\odot}$  ( $\pm 0.05 M_{\odot}$ ), preferring the high-mass solutions around  $1.51 M_{\odot}$  from the PAT\_P04\_OPT and PAT\_STS patterns. The core hydrogen fraction we find to be between 0.42 and 0.49 ( $\pm 0.04$ ). The lower values correspond to the preferred PAT\_P04\_OPT and PAT\_LI2020 patterns; we also note that core hydrogen fractions no higher than 0.58 are permitted based on the intersecting radius and spectroscopic constraints. Stellar radii we find to be between  $1.55 R_{\odot}$  and  $1.68 R_{\odot}$  (with uncertainties no higher than  $\pm 0.1 R_{\odot}$ ), preferring the higher radius solutions from the PAT\_P04\_OPT and PAT\_STS patterns, which we note are more consistent with the eclipse modelling from Kemp et al. (2024). The metallicity shows, for all patterns and constraints, a preference to the lower metallicity bound of C-3P0. This is consistent with atmospheric modelling estimates for the metallicity from Kemp et al. (2024), which place the star slightly below the metallicity range able to be modelled by C-3P0. The best-fitting models consistently prefer low values of exponential overshooting regardless of the pattern or constraint considered. This is consistent with the low-mass end of the empirical  $M\text{-}f_{\text{ov}}$  relation for  $\gamma$  Dor stars put forth by Claret & Torres (2017), as well as the probability distributions for  $\gamma$  Dor stars computed by Mombarg et al. (2024a).

The best fitting models have  $T_{\text{eff}}$  between 7160 K and 7180 K, placing them just below the  $1\text{-}\sigma$  uncertainty region from the spectroscopic analysis ( $7280 \pm 70 \text{ K}$ ). The uncertainty estimates for  $\log(T_{\text{eff}})$  of approximately  $\pm 0.008$  dex are sufficient to overlap with the spectroscopic solution. Helped considerably by the intersecting radius and spectroscopic constraints, the best-fitting models have  $\log(g)$  varying between 4.168 dex and 4.223 dex ( $\pm 0.04$  dex), with the preferred PAT\_P04\_OPT and PAT\_LI2020 fits arriving at results at the lower end of the range. We find that  $\log(L)$ , also helped considerably by the intersecting spectroscopic and radius constraints, is between 0.745 dex and 0.819 dex ( $\pm 0.005$  dex), preferring the high luminosity solutions from the PAT\_P04\_OPT and PAT\_STS patterns. These higher solutions are consistent with the stellar luminosity calculated from *Gaia* DR3 and light fractions for Aa from Kemp et al. (2024) and Helminiak et al. (2017).

We estimate the age of Aa to be approximately  $1100 \pm 100$  Myr, much older than the 35 Myr age implied by Helminiak et al. (2017)’s isochrone fits. This older age from asteroseismology is also supported by the radius measurement from Kemp et al. (2024), and serves as a reminder of the important role that asteroseismology can play in stellar parameter estimation.

From our parameter-based MCMC grid-search, we were able to recover similar solutions for the stellar parameters of KIC 4150611 Aa, including the stellar age. Comparing differ-



ent model grids, the significant effect of metallicity on the buoyancy travel time was evident. The need for careful treatment of the envelope mixing was also evident, potentially affecting the buoyancy travel by as much as the metallicity.

As future work it would be interesting to revisit the isochrone fitting of the B system in an attempt to confirm its age, ideally in parallel with an independent isochrone aging of the components of the A triple system using their radii and estimated seismic masses. KIC 4150611 is not part of a particularly crowded field, so the fact that there are four sets of eclipses is highly suggestive of a physical association, and likely a co-evolutionary origin, between its A, B, and C components. A revisit of the aging of different system components could provide clarity on this issue, and greatly assist in establishing the evolution history of this fascinating system.

*Acknowledgements.* The authors wish to thank Sarah Gebruers, Dominic Bowman, and Annachiara Picco for their useful discussion and input. The research leading to these results has received funding from the KU Leuven Research Council (grant C16/18/005: PARADISE), from the Research Foundation Flanders (FWO) under grant agreement G089422N (AT, CA) and 1124321N (LIJ), as well as from the Belgian federal Science Policy Office (BELSPO) through PRODEX grant PLATO. V.V. gratefully acknowledges support from the Research Foundation Flanders (FWO) under grant agreement N°1156923N (PhD Fellowship). JSGM acknowledges funding the French Agence Nationale de la Recherche (ANR), under grant MASSIF (ANR-21-CE31-0018-02). CA acknowledges funding by the European Research Council under grant ERC SyG 101071505. Funded by the European Union. Views and opinions expressed are however those of the author(s) only and do not necessarily reflect those of the European Union or the European Research Council. Neither the European Union nor the granting authority can be held responsible for them. This paper includes data collected by the Kepler mission, which are publicly available from the Mikulski Archive for Space Telescopes (MAST) at the Space Telescope Science Institute (STScI). Funding for the Kepler mission is provided by the NASA Science Mission Directorate. STScI is operated by the Association of Universities for Research in Astronomy, Inc., under NASA contract NAS 5–26555.

## References

- Aerts, C. 2021, *Reviews of Modern Physics*, 93, 015001
- Aerts, C., Christensen-Dalsgaard, J., & Kurtz, D. W. 2010, *Asteroseismology* (Springer)
- Aerts, C., Molenberghs, G., Michielsen, M., et al. 2018, *ApJS*, 237, 15
- Aerts, C. & Tkachenko, A. 2024, *A&A*, in press, arXiv:2311.08453
- Aerts, C., Van Reeth, T., Mombarg, J. S. G., & Hey, D. 2024, *A&A*, submitted
- Aerts, C., Waelkens, C., Daszyńska-Daszkiewicz, J., et al. 2004, *A&A*, 415, 241
- Asplund, M., Grevesse, N., Sauval, A. J., & Scott, P. 2009, *ARA&A*, 47, 481
- Baglin, A. 2003, *Advances in Space Research*, 31, 345
- Balona, L. A. 2014, *MNRAS*, 443, 1946
- Baran, A. S., Koen, C., & Pokrzywka, B. 2015, *MNRAS*, 448, L16
- Berthomieu, G., Gonczi, G., Graff, P., Provost, J., & Rocca, A. 1978, *A&A*, 70, 597
- Borucki, W. J., Koch, D., Basri, G., et al. 2010, *Science*, 327, 977
- Bouabid, M. P., Dupret, M. A., Salmon, S., et al. 2013, *MNRAS*, 429, 2500
- Claret, A. & Torres, G. 2017, *ApJ*, 849, 18
- De Cat, P. & Aerts, C. 2002, *A&A*, 393, 965
- De Cat, P., Eyser, L., Cuypers, J., et al. 2006, *A&A*, 449, 281
- Degroote, P., Aerts, C., Ollivier, M., et al. 2009, *A&A*, 506, 471
- Dupret, M. A., Grigahcène, A., Garrido, R., Gabriel, M., & Scuflaire, R. 2005, *A&A*, 435, 927
- Eckart, C. 1960, *Physics of Fluids*, 3, 421
- Freytag, B., Ludwig, H. G., & Steffen, M. 1996, *A&A*, 313, 497
- Fritzewski, D. J., Aerts, C., Mombarg, J. S. G., Gossage, S., & Van Reeth, T. 2024, *A&A*, 684, A112
- Gaia Collaboration, Prusti, T., de Bruijne, J. H. J., et al. 2016, *A&A*, 595, A1
- Gaia Collaboration, Vallenari, A., Brown, A. G. A., et al. 2023, *A&A*, 674, A1
- Gebruers, S., Straumit, L., Tkachenko, A., et al. 2021, *A&A*, 650, A151
- Helminiak, K. G., Ukita, N., Kambe, E., et al. 2017, *A&A*, 602, A30
- Herwig, F. 2000, *A&A*, 360, 952
- Hough, S. S. 1898, *Philosophical Transactions of the Royal Society of London Series A*, 191, 139
- Ijspeert, L. W., Tkachenko, A., Johnston, C., et al. 2024, *A&A*, 685, A62
- Johnson, R. A., Wichern, D. W., et al. 2019, *Applied multivariate statistical analysis* (Prentice hall Upper Saddle River, NJ)
- Johnston, C., Tkachenko, A., Aerts, C., et al. 2019, *MNRAS*, 482, 1231
- Kemp, A., Tkachenko, A., Torres, G., et al. 2024, arXiv e-prints, arXiv:2406.04131
- Lee, U. & Saio, H. 1989, *MNRAS*, 237, 875
- Lee, U. & Saio, H. 1997, *ApJ*, 491, 839
- Li, G., Aerts, C., Bedding, T. R., et al. 2024, *A&A*, 686, A142
- Li, G., Bedding, T. R., Murphy, S. J., et al. 2019a, *MNRAS*, 482, 1757
- Li, G., Guo, Z., Fuller, J., et al. 2020a, *MNRAS*, 497, 4363
- Li, G., Van Reeth, T., Bedding, T. R., Murphy, S. J., & Antoci, V. 2019b, *MNRAS*, 487, 782
- Li, G., Van Reeth, T., Bedding, T. R., et al. 2020b, *MNRAS*, 491, 3586
- Lomb, N. R. 1976, *Ap&SS*, 39, 447
- Mathis, S. 2009, *A&A*, 506, 811
- Mathis, S., Talon, S., Pantillon, F. P., & Zahn, J. P. 2008, *Sol. Phys.*, 251, 101
- Michielsen, M. 2024, *Journal of Open Source Software*, 9, 5884
- Michielsen, M., Aerts, C., & Bowman, D. M. 2021, *A&A*, 650, A175
- Michielsen, M., Van Reeth, T., Tkachenko, A., & Aerts, C. 2023, *A&A*, 679, A6
- Miglio, A., Montalbán, J., Noels, A., & Eggenberger, P. 2008, *MNRAS*, 386, 1487
- Mombarg, J. S. G., Aerts, C., & Molenberghs, G. 2024a, *A&A*, 685, A21
- Mombarg, J. S. G., Aerts, C., Van Reeth, T., & Hey, D. 2024b, arXiv e-prints, arXiv:2410.05367
- Mombarg, J. S. G., Van Reeth, T., & Aerts, C. 2021, *A&A*, 650, A58
- Mombarg, J. S. G., Van Reeth, T., Pedersen, M. G., et al. 2019, *MNRAS*, 485, 3248
- Niemczura, E., Murphy, S. J., Smalley, B., et al. 2015, *MNRAS*, 450, 2764
- Ogilvie, G. I. & Lin, D. N. C. 2004, *ApJ*, 610, 477
- Paxton, B., Cantiello, M., Arras, P., et al. 2013, *ApJS*, 208, 4
- Pecaut, M. J. & Mamajek, E. E. 2013, *ApJS*, 208, 9
- Pedersen, M. G., Aerts, C., Pápics, P. I., et al. 2021, *Nature Astronomy*, 5, 715
- Prša, A., Batalha, N., Slawson, R. W., et al. 2011, *AJ*, 141, 83
- Ricker, G. R., Winn, J. N., Vanderspek, R., et al. 2015, *Journal of Astronomical Telescopes, Instruments, and Systems*, 1, 014003
- Rowe, J. F., Coughlin, J. L., Antoci, V., et al. 2015, *ApJS*, 217, 16
- Scargle, J. D. 1982, *ApJ*, 263, 835
- Schmid, V. S. & Aerts, C. 2016, *A&A*, 592, A116
- Shaviv, G. & Salpeter, E. E. 1973, *ApJ*, 184, 191
- Shibahashi, H. 1979, *PASJ*, 31, 87
- Shibahashi, H. & Kurtz, D. W. 2012, *MNRAS*, 422, 738
- Szentgyorgyi, A. H. & Fűrész, G. 2007, in *Revista Mexicana de Astronomía y Astrofísica Conference Series*, Vol. 28, *Revista Mexicana de Astronomía y Astrofísica Conference Series*, ed. S. Kurtz, 129–133
- Tassoul, M. 1980, *ApJS*, 43, 469
- Tkachenko, A. 2015, *A&A*, 581, A129
- Townsend, R. H. D. 2020, *MNRAS*, 497, 2670
- Townsend, R. H. D. & Teitler, S. A. 2013, *MNRAS*, 435, 3406
- Triana, S. A., Moravveji, E., Pápics, P. I., et al. 2015, *ApJ*, 810, 16
- Uytterhoeven, K., Moya, A., Grigahcène, A., et al. 2011, *A&A*, 534, A125
- Van Beeck, J., Bowman, D. M., Pedersen, M. G., et al. 2021, *A&A*, 655, A59
- Van Reeth, T., De Cat, P., Van Beeck, J., et al. 2022, *A&A*, 662, A58
- Van Reeth, T., Johnston, C., Southworth, J., et al. 2023, *A&A*, 671, A121
- Van Reeth, T., Mombarg, J. S. G., Mathis, S., et al. 2018, *A&A*, 618, A24
- Van Reeth, T., Tkachenko, A., & Aerts, C. 2016, *A&A*, 593, A120
- Van Reeth, T., Tkachenko, A., Aerts, C., et al. 2015a, *A&A*, 574, A17
- Van Reeth, T., Tkachenko, A., Aerts, C., et al. 2015b, *ApJS*, 218, 27
- Zahn, J. P. 1991, *A&A*, 252, 179

## Appendix A: Detailed period-spacing pattern plots

## Appendix B: Tight $R$ constraint

## Appendix C: Other frequency groups

The focus of this work has been asteroseismic exploitation of a dipole prograde gravito-inertial mode period-spacing pattern. However, there are some additional smaller groups of frequencies within the Fourier spectrum. Here, we briefly describe these features and speculate on their potential utility in the context of future, more refined modelling attempts.

Between 0.1 d and 0.28 d in the periodogram, there are a large number of statistically significant periods where we expect quadrupole and septupole series to appear (around 0.14 d and 0.2 d, respectively). There is a great deal of contamination, however, and only a few consecutive periods in a (probable) quadrupole pattern can be identified. The relevant extracted frequencies are shown in Fig. C.1. These series did not feature as part of our analysis, the main component of which relied on asteroseismic models of prograde dipole modes.

As previously noted by Helminiak et al. (2017), there are several low-frequency cones present in the Fourier spectrum around  $0.19 \text{ d}^{-1}$ ,  $0.38 \text{ d}^{-1}$ , and  $0.56 \text{ d}^{-1}$ , with the two higher frequency cones presumably being harmonics relating to the dominant  $0.19 \text{ d}^{-1}$  cone. These cones are shown in Figure C.2. Helminiak et al. (2017) propose that the  $0.18 \text{ d}^{-1}$  is caused by rotation one or both of the two G stars Ba and Bb, commenting that the complicated structure of these peaks could be a result of either differential rotation or originate from two stars rotating at similar rates. From atmospheric modelling of the disentangled spectra in Kemp et al. (2024), the rotation rates for Ba and Bb were estimated to be  $v_{\sin(i)} = 8.9 \pm 1.1 \text{ km s}^{-1}$  and  $v_{\sin(i)} = 9.2 \pm 1.1 \text{ km s}^{-1}$ , respectively. From Helminiak et al. (2017), we also have estimates for the stellar radii for the Ba and Bb of  $0.888 \pm 0.010 R_{\odot}$  and  $0.856 \pm 0.038 R_{\odot}$ , respectively. Assuming rigid rotation, this corresponds to rotation frequencies of approximately  $0.2 \pm 0.02 \text{ d}^{-1}$  and  $0.21 \pm 0.03 \text{ d}^{-1}$ . This is slightly higher than expected from the centre of the cone, although within uncertainty. It is likely that even a small systematic error in either the rotation velocity or the radius estimate could resolve this. We note that in the scenario of differential rotation, an offset between the surface rotation and the interior might be expected. However, according to our surface rotation estimate the surface would be rotating slightly faster than the interior, and significantly faster than the orbital frequency of the eccentric B binary ( $0.116 \text{ d}^{-1}$ ). We conclude that the rotation of the B stars is almost certainly the cause of these cones, noting that the surface rotation rate is consistent with the cone frequencies to within  $1 - \sigma$ .

Finally, there are the high-amplitude p-modes at  $17.75 \text{ d}^{-1}$ ,  $18.48 \text{ d}^{-1}$ ,  $20.24 \text{ d}^{-1}$ , and  $22.62 \text{ d}^{-1}$  (see Fig. 4). They exhibit significant, symmetric splitting that is present after prewhitening. The splitting corresponds to the orbital frequency of the Aa binary, and may be due to light travel-time effects. Similar splittings are only occasionally visible in the g-mode regime, but are but are never statistically significant even for the high-amplitude peaks. There is no sign of rotational splitting.

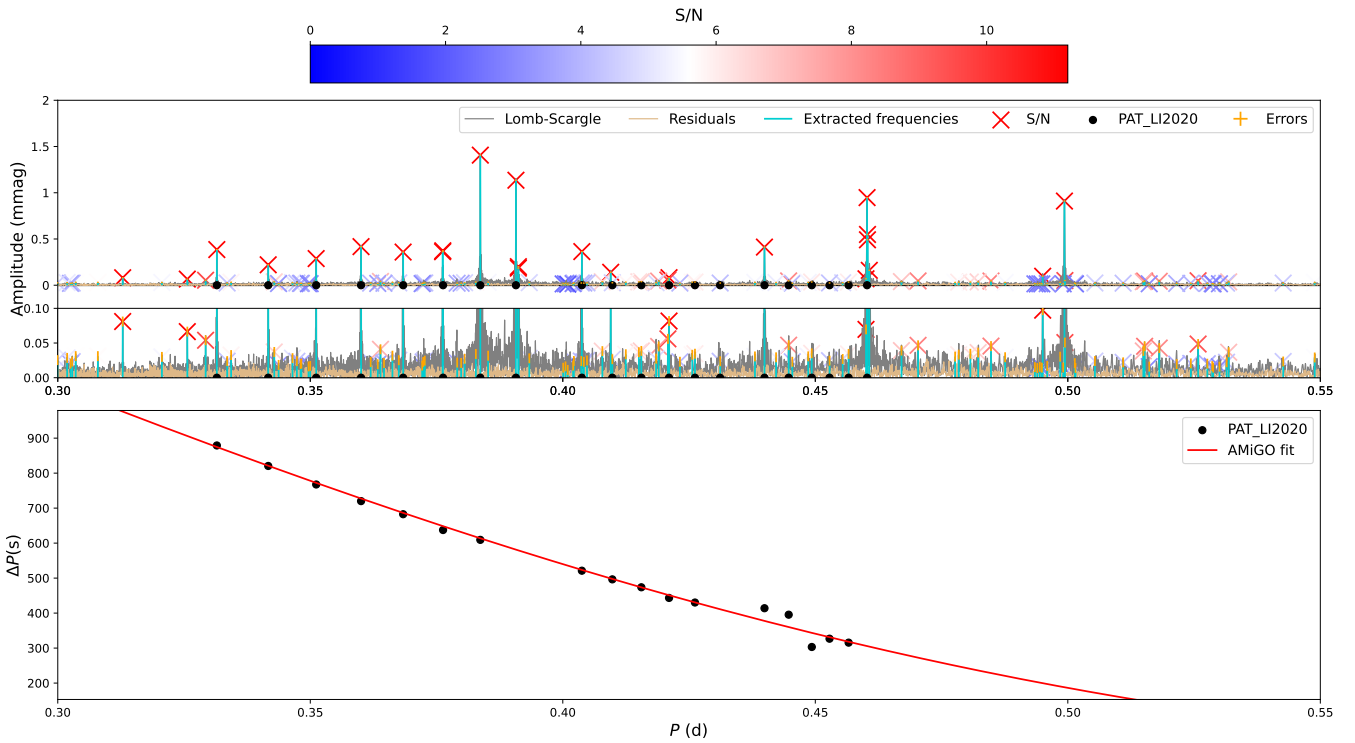


Fig. A.1: PAT\_LI2020 period-spacing pattern from Li et al. (2020a). The Lomb-Scargle periodogram is shown in grey, the extracted frequencies in light blue, and the residual periodogram with the extracted frequencies removed in orange. Orbital harmonics are excluded. The SNR ratio is indicated by the colour of the ‘X’ symbol for each extracted frequency, while the amplitude and period errors (more easily seen in the inset panel, which better shows the low-amplitude behaviour) are shown in orange. The extracted frequencies selected to be part of the pattern are marked with a filled black circle. Note that only the black point and the AMiGO fit and predictions are specifically related to the PAT\_LI2020 pattern; the Lomb-Scargle periodogram and its residuals, as well as the extracted frequencies (and their associated SNR and errors), are included from the `period04` extraction for comparison purposes.

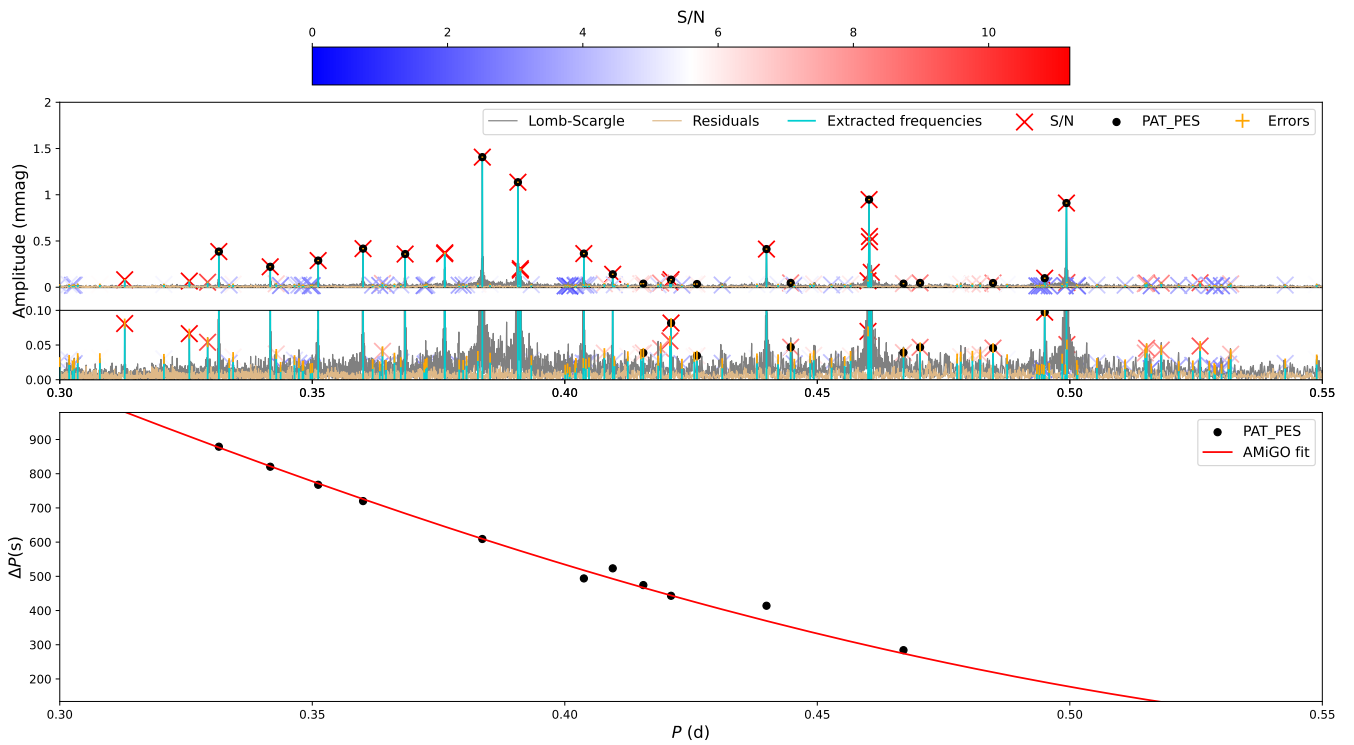


Fig. A.2: PAT\_P04\_PES period-spacing pattern. Orbital harmonics are excluded. The high-amplitude period at 0.36d is excluded in this pattern only due to its near-perfect coincidence with an 8.65d orbital harmonic. A detailed description of all symbols and information can be found in Figure A.1.

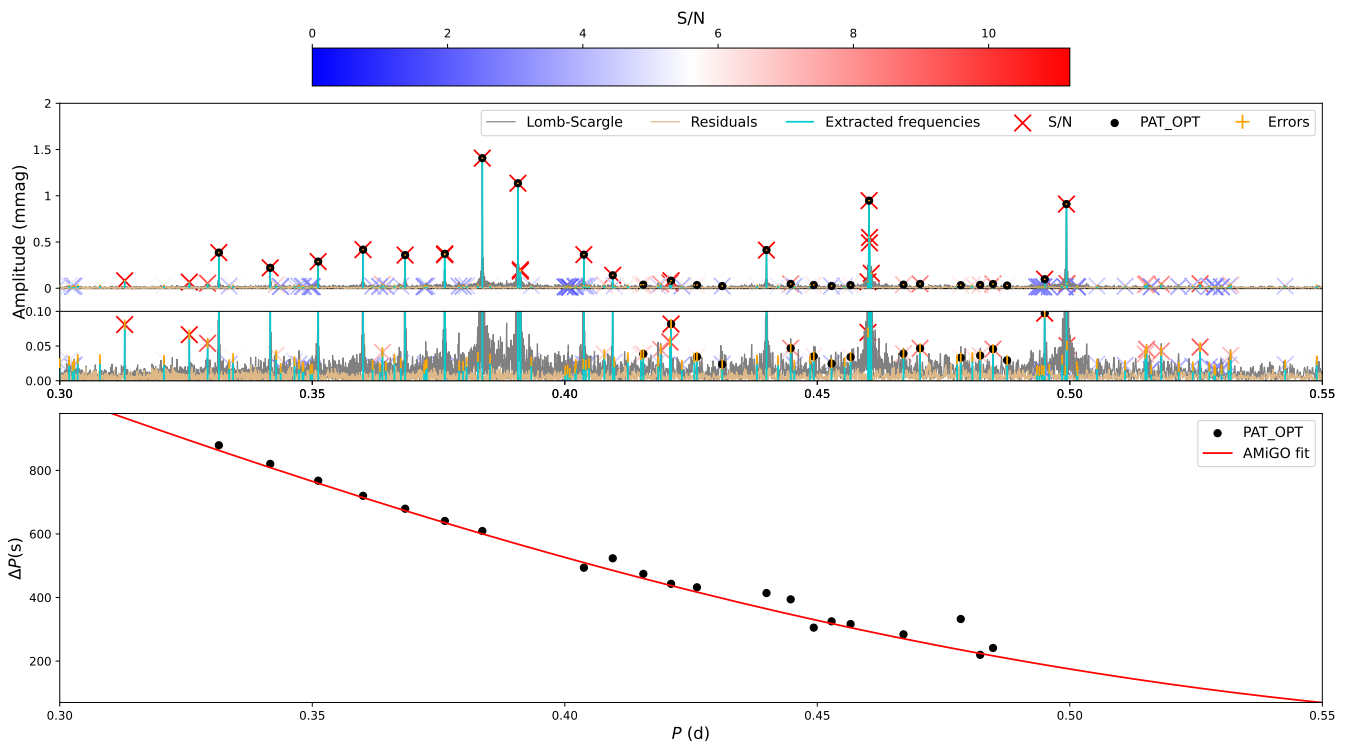


Fig. A.3: PAT\_P04\_OPT period-spacing pattern. Orbital harmonics are excluded. A detailed description of all symbols and information can be found in Figure A.1.

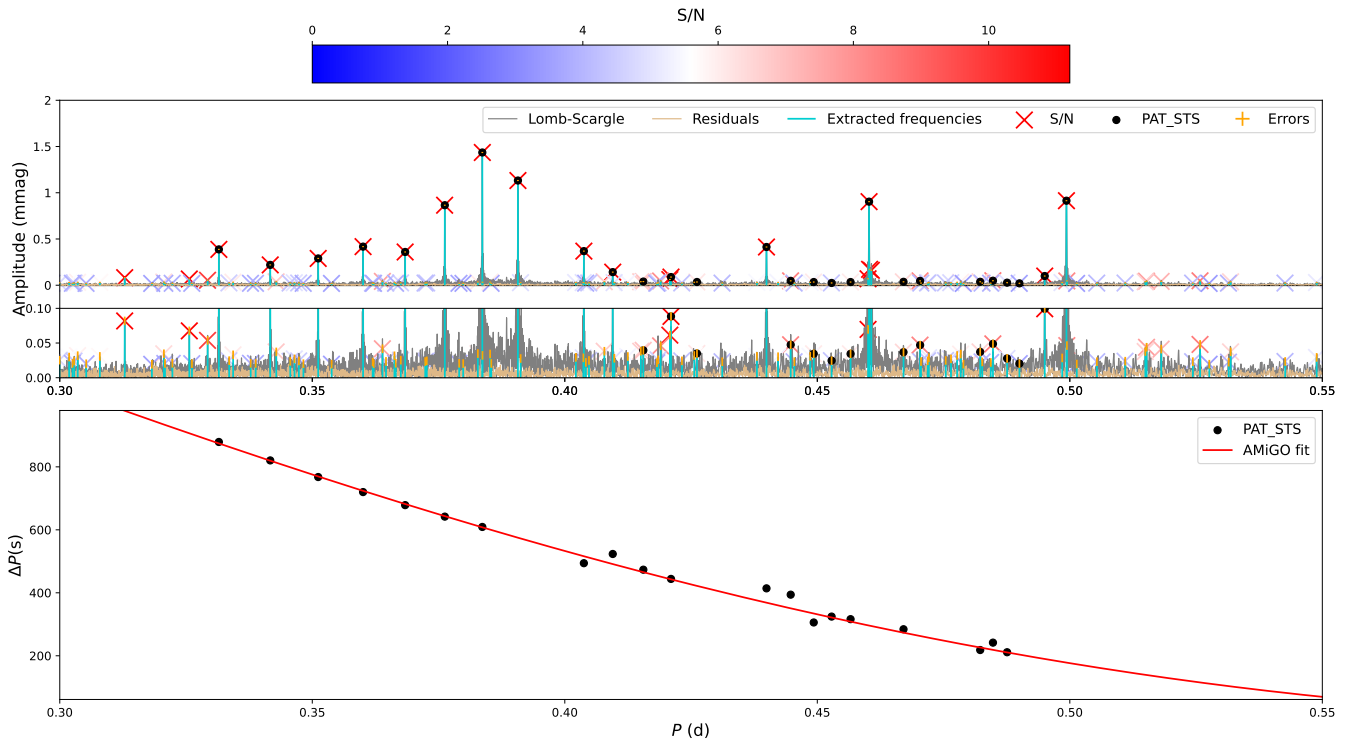


Fig. A.4: PAT\_STS period-spacing pattern. Orbital harmonics are excluded. A detailed description of all symbols and information can be found in Figure A.1.



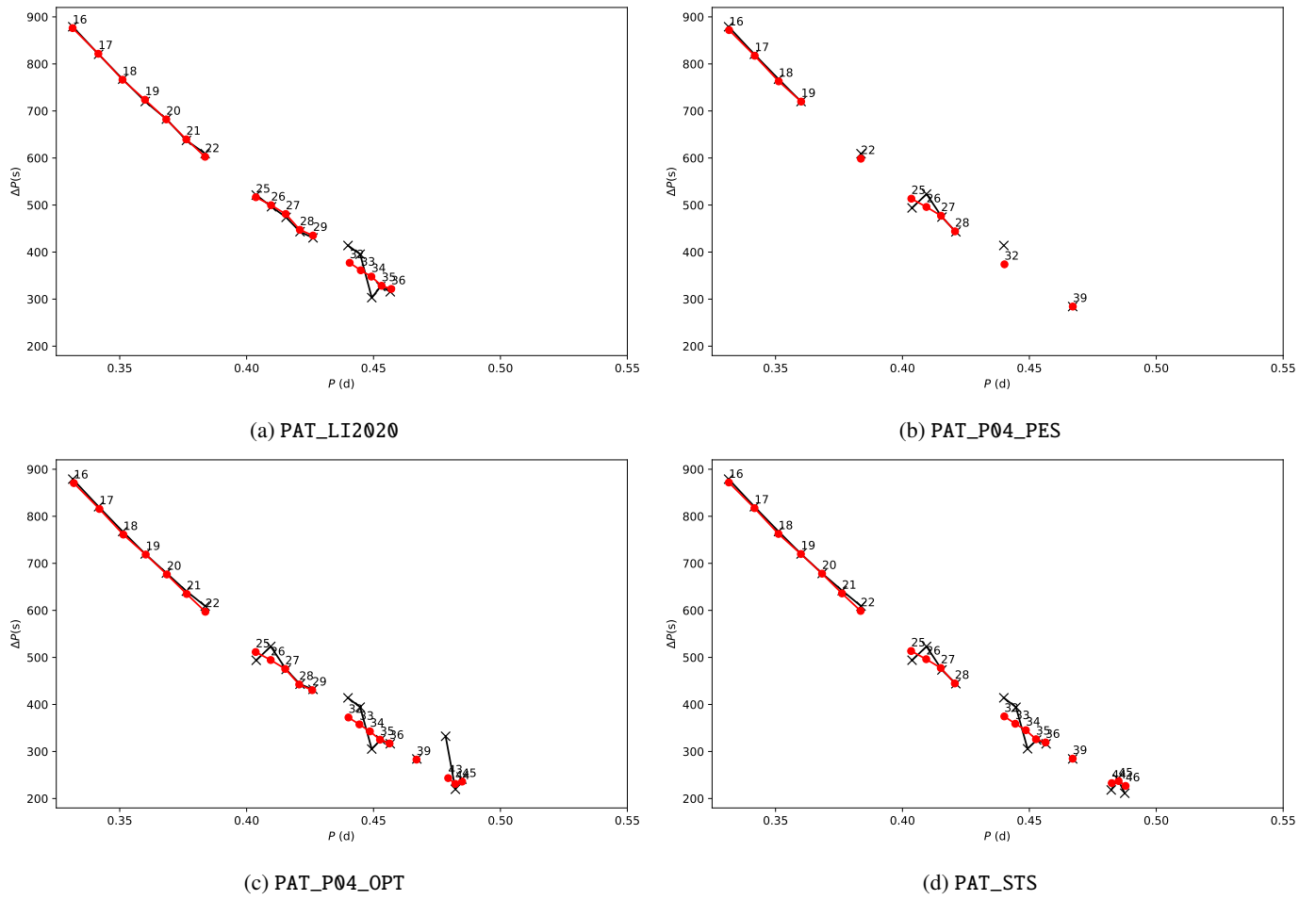


Fig. B.1: Best-fitting C-3P0 models (red) consistent with the tight and spectroscopic constraints from the high resolution sampling. Observed patterns are shown in black.

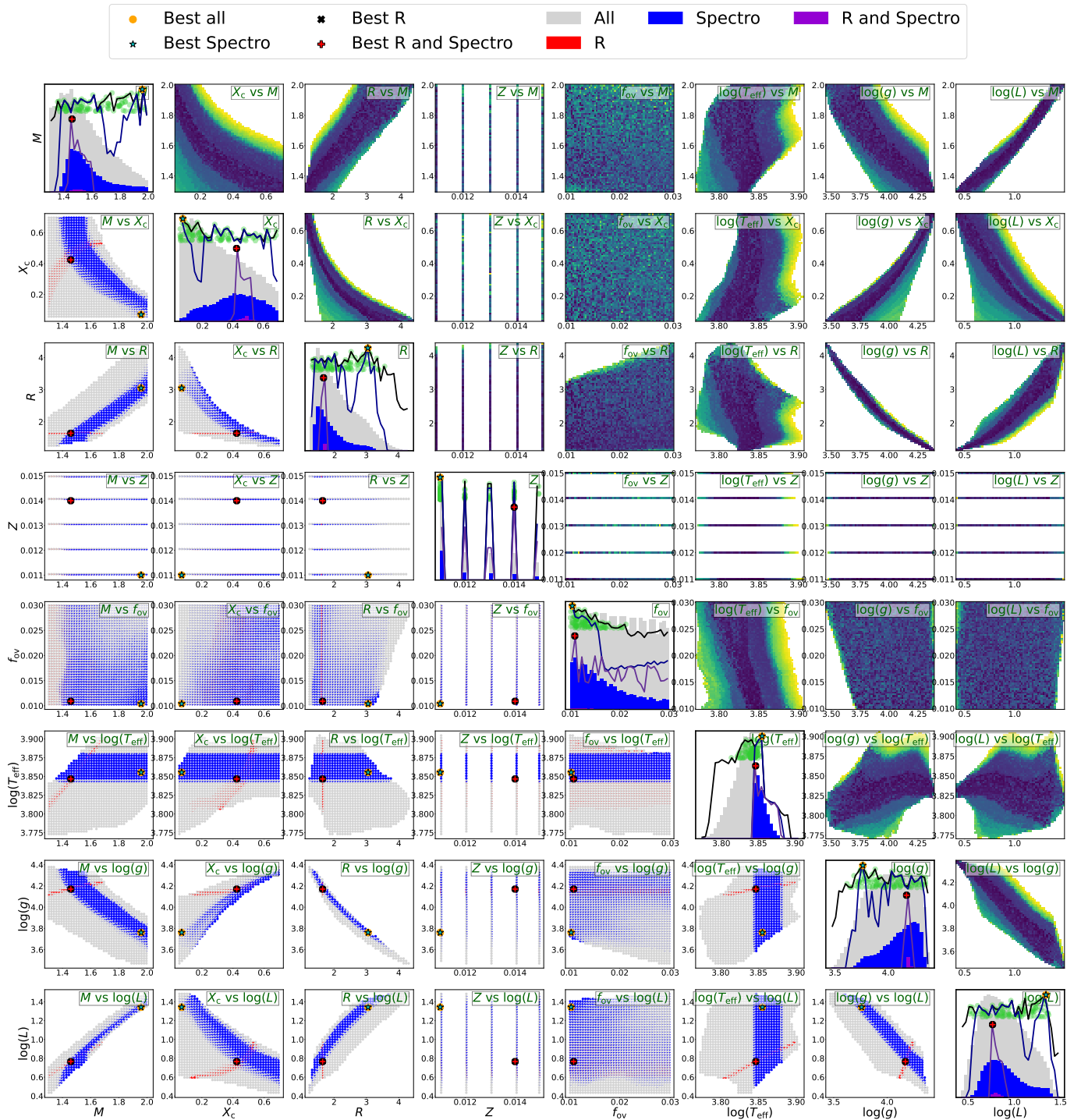


Fig. B.2: PAT\_LI2020 PAT\_P04\_PES modelling results, tight radial constraint. See Fig. 8 for detailed description of the different plot elements.

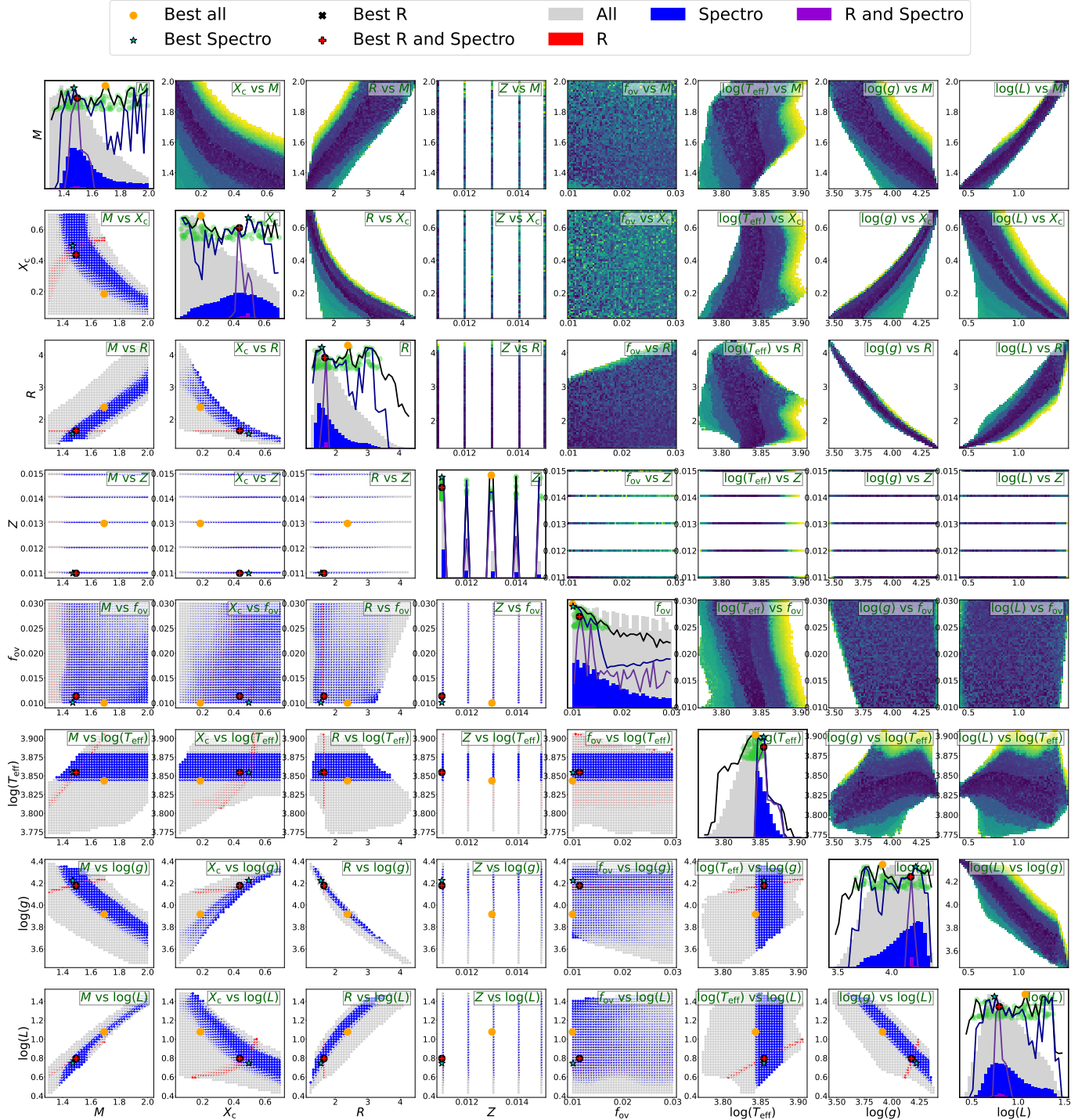


Fig. B.3: PAT\_P04\_PES modelling results, tight radial constraint. See Fig. 8 for detailed description of the different plot elements.

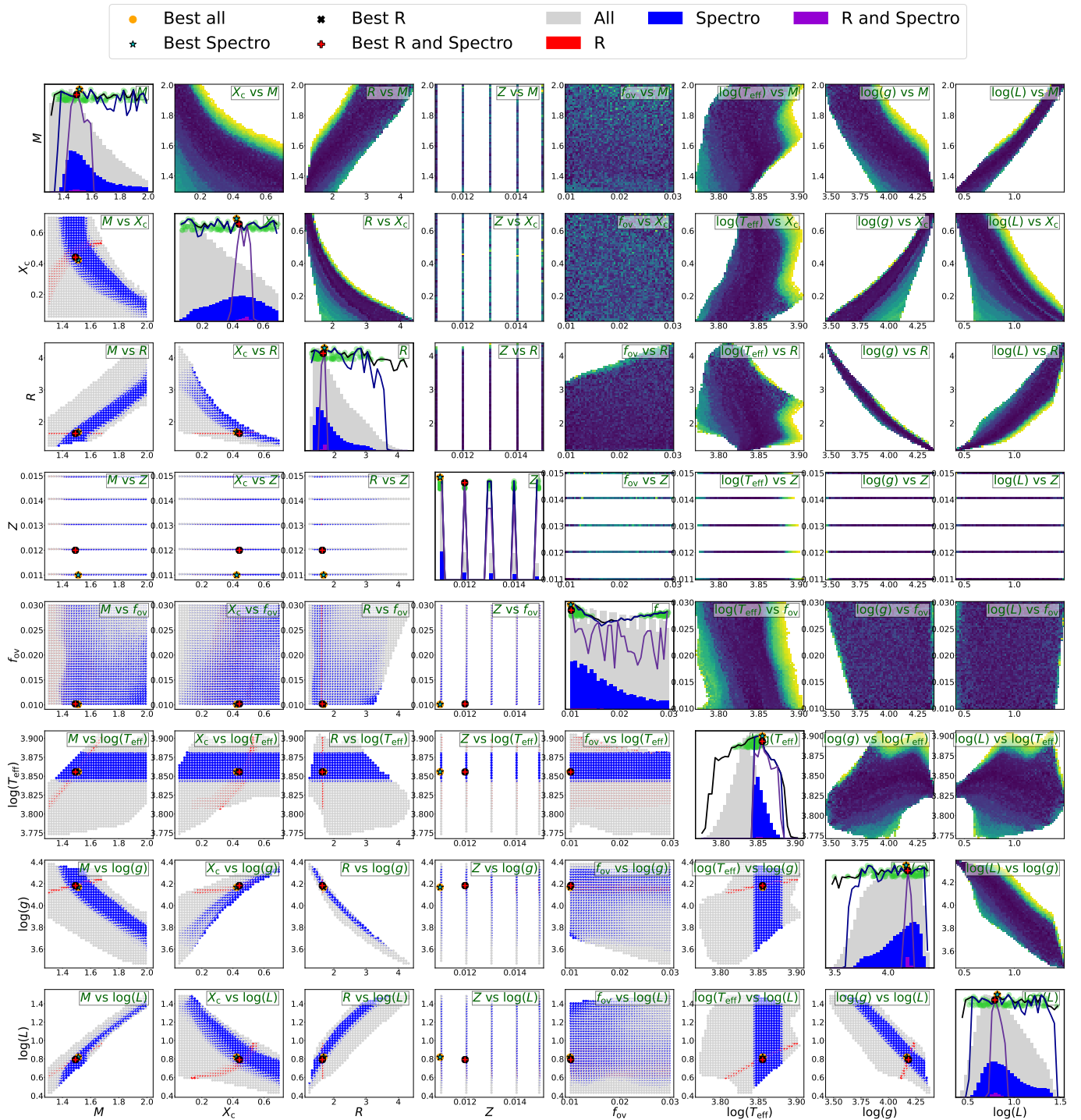


Fig. B.4: PAT\_P04\_OPT modelling results, tight radial constraint. See Fig. 8 for detailed description of the different plot elements.



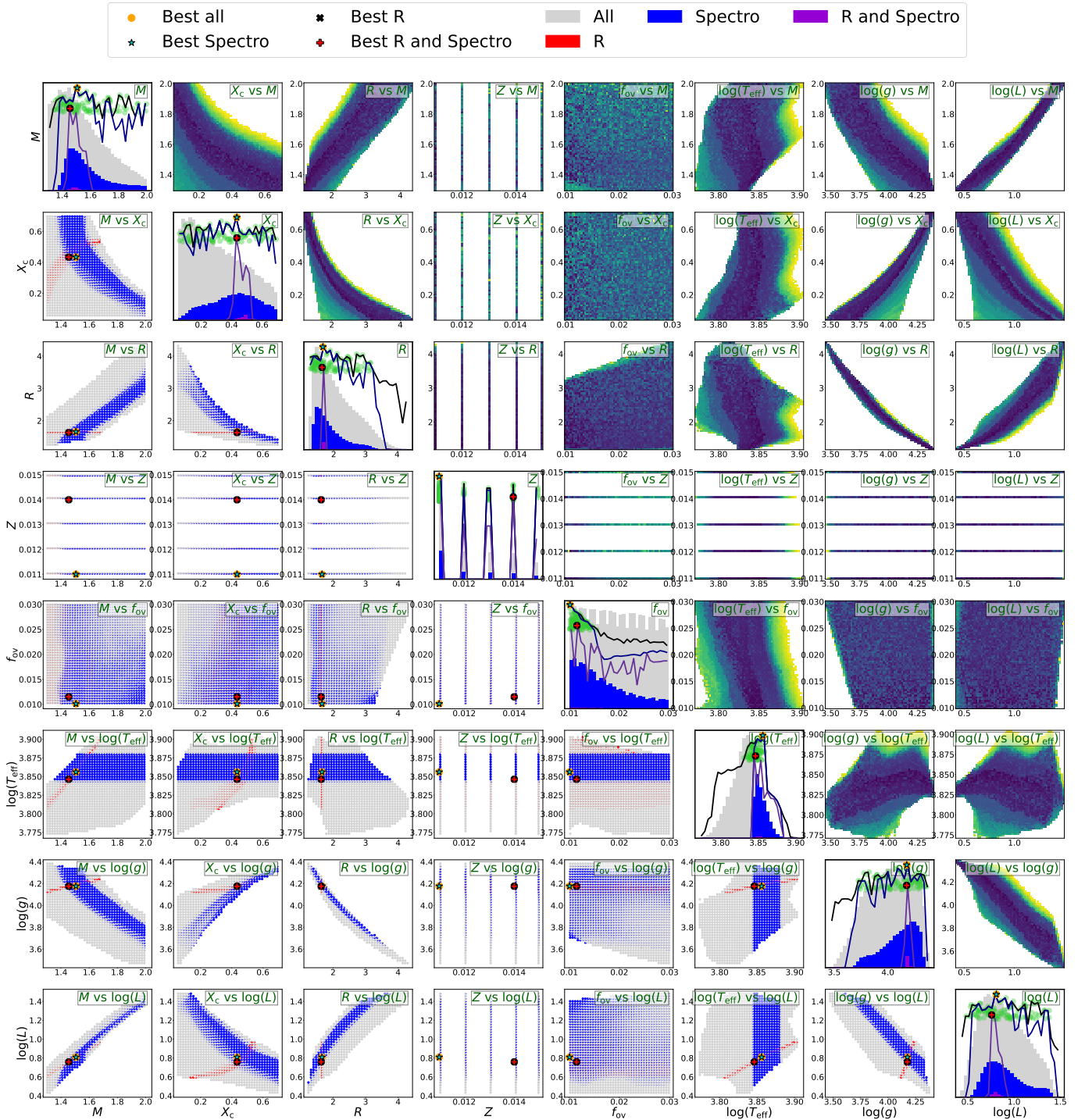


Fig. B.5: PAT\_STS modelling results, tight radial constraint. See Fig. 8 for detailed description of the different plot elements.



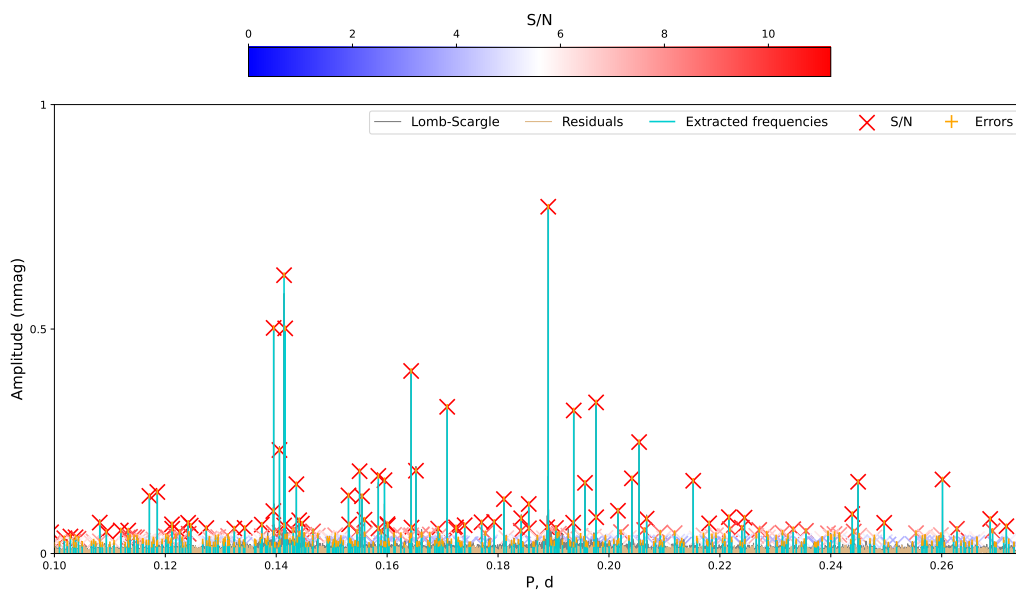


Fig. C.1: Likely high order g-modes, shown in the period domain. The cluster around 0.2 d are where we expect the  $l=2$  series to appear, while those around 0.14 are likely the  $l=3$  series. At most, a very short (perhaps 2-3 consecutive spacings) might be confidently obtained from the  $l = 2$  series.

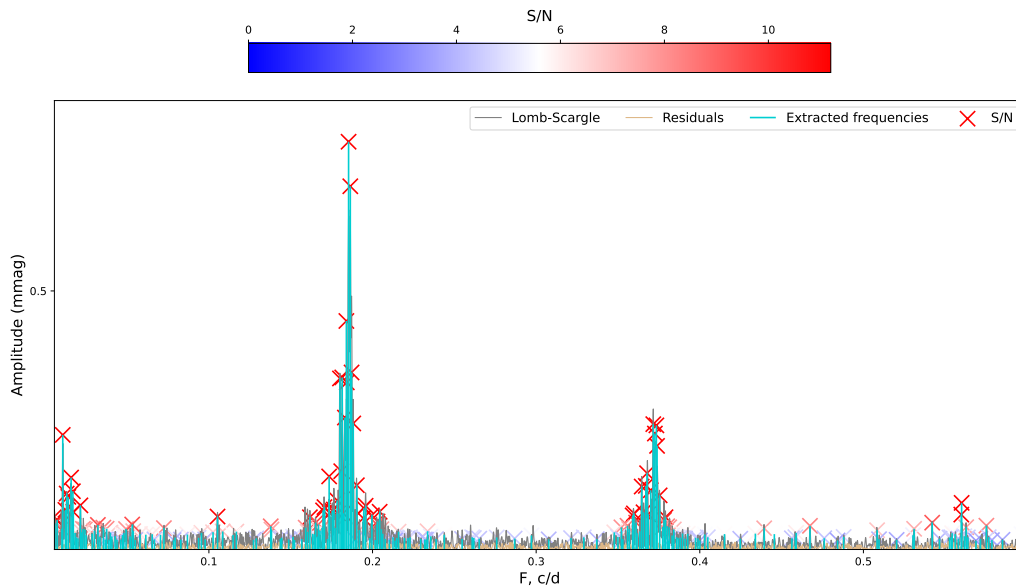


Fig. C.2: Series of low-frequency cones around 0.19, 0.38, and  $0.56 \text{ d}^{-1}$ . Origin of these frequency cones is unknown, and does not appear to coincide with any of the existing periods or known rotation rates.